



The hypersonic inlet buzz evolution under the fluid-structure interaction effect with a flexible plate

Kun Ye 1,2,3 , Yanqiu Guo 1,2,3 , Xinxin Zhou 1,2,3 , Hengsheng Zhang 1,4 and Zhengyin Ye 1,2,3

Corresponding author: Kun Ye, yekun@nwpu.edu.cn

(Received 17 September 2024; revised 19 July 2025; accepted 17 August 2025)

For hypersonic inlets, buzz is a self-sustained oscillatory flow characterised by strong nonlinear and unsteady behaviour. Our recent study shows that, unlike conventional alterations in flow conditions at the inlet entrance or exit, flexible lip deformation is a newly identified trigger for buzz. However, the mechanism by which this fluid-structure interaction (FSI) behaviour induces buzz remains unclear. To clarify how FSI acts as a dominant factor in triggering flow instability leading to buzz, this study investigates a more general flexible plate model within the inlet. The results show that the plate FSI introduces a prolonged instability accumulation process for buzz evolution, resulting in a 'gradual-onset' characteristic differing from previous studies. During this process, plate FSI amplifies downstream flow oscillations while accumulating unstable energy. Eventually, the excessive unstable energy causes the shock train to destabilise and be disgorged from the inlet, initiating a complete instability process dominated by buzz. Notably, buzz induced by plate FSI exhibits unsteady characteristics similar to those observed in rigid inlets. Therefore, as an internal self-excited disturbance source, plate FSI produces relatively weaker disturbances than conventional flow modifications, but exhibits highly persistent accumulation effects and distinct multistage characteristics. This study reveals the buzz evolution mechanism under plate FSI, providing new insights into flow instability in hypersonic inlets.

Key words: hypersonic flow, flow-structure interactions, shock waves

¹School of Aeronautics, Northwestern Polytechnical University, Xi'an, 710072, PR China

²National Key Laboratory of Aircraft Configuration Design, Xi'an, 710072, PR China

³Institute of Extreme Mechanics, Northwestern Polytechnical University, Xi'an, 710072, PR China

⁴Aircraft Strength Research Institute of China, Xi'an, 710065, PR China

1. Introduction

The hypersonic inlet is a critical aerodynamic component of a scramjet (Sziroczak & Smith 2016). Its shock system decelerates and compresses the high-speed incoming flow to a reasonable exit velocity, ensuring the normal and efficient operation of the scramjet. However, under conditions such as excessively low incoming Mach numbers, high angles of attack, or elevated downstream combustor back pressure (Baccarella et al. 2021; Khobragade, Unnikrishnan & Kumar 2022), the inlet flow may exhibit self-sustained oscillations, during which the internal shock system is periodically disgorged and swallowed. This unsteady flow phenomenon is known as 'buzz'. Buzz is highly destructive, significantly impairing the performance and structural safety of scramjets, and may even lead to flight accidents (Chang et al. 2018; Im & Do 2018).

In recent years, significant research has been devoted to hypersonic inlet buzz. Under different throttling ratios, Tan et al. (2009) identified two types of buzz patterns: relatively mild 'little buzz' and highly violent 'big buzz'. 'Little buzz' is characterised by the oscillatory motion of the oblique shock on the ramp side, while 'big buzz' features the periodic disruption and reconstruction of the oblique shocks and shock train within the inlet. Moreover, 'big buzz' exhibits intermittency, with brief periods of stable flow occurring randomly during the buzz process. Additionally, by increasing throttling ratios, Wagner et al. (2009) observed three buzz patterns: high-amplitude buzz, non-oscillatory unstart flow, and low-amplitude buzz. Both high-amplitude buzz and low-amplitude buzz are associated with shock trains downstream of the isolator. Chang et al. (2012) extended the Mach number range of the experiments. They observed two novel buzz patterns. One is a mixed oscillatory pattern that combines 'big buzz' with 'little buzz', and the other is a non-oscillatory violent pattern. The latter exhibits the same intermittency mentioned by Tan et al. (2009). From a flow structure perspective, Zhang et al. (2016a,b) analysed the dominant factors of two buzz patterns under different Mach numbers. Subsequently, by decreasing throttling ratios, Huang et al. (2021) found buzz flow during the restart of the inlet. This buzz flow can be classified into two patterns: stable buzz and intermittent buzz. Besides buzz patterns, researchers have also shown considerable interest in buzz frequency. Li et al. (2013) found that the buzz frequency increases with increasing throttling ratio. The speed of the upstream-propagating shock within the inlet significantly affects buzz frequency. Zhang et al. (2016a,b) discovered that when buzz flow with dominant frequency 30 Hz occurs, there is a temporary reverse airflow in the contracting part of the inlet. Meanwhile, two secondary high-frequency oscillation modes appear at 360 and 900-1300 Hz. Berto et al. (2020) found that buzz flow activates high-amplitude pressure oscillations at both low and high frequencies. Under such buzz conditions, the Ferri and Dailey criteria exist simultaneously. Further, Devaraj et al. (2021) defined the boundary between the two criteria. These studies indicate that the hypersonic inlet buzz flow is complex. By changing the flow conditions at the inlet entrance or exit, buzz exhibits different oscillation patterns and frequency characteristics. It also displays features such as intermittency and randomness.

However, an implicit assumption in most of these studies is that the inlet structures are rigid. In reality, due to the lightweight structural design, the stiffness of hypersonic inlet structures is significantly reduced. Under aerodynamic loads, the inlet is prone to unpredictable deformation, leading to fluid–structure interaction (FSI) issues. Through numerical simulation, Kline *et al.* (2014) studied the impact of static aerothermoelastic deformation on the inlet performance. They found that a vertical deflection of 0.165 mm at the front end of the inlet produces a 4.5 % change in thrust. Subsequently, Lamorte *et al.* (2015) developed an uncertainty quantification framework in numerical simulations, and identified lip deformation as a critical factor affecting inlet performance. Ye *et al.* (2019)

further analysed the flowfield structure under lip deformation. Significant deformation alters nearby shock structures, enhances internal shock intensity, and extends separation zones. These changes lead to pulsations in performance parameters. Through experiments, Bhattrai et al. (2022) found that the total pressure recovery of an inlet with a flexible ramp decreased by 20% compared to a rigid model. Additionally, a 6% deformation of the inlet ramp leads to unstart. Previous studies have shown that even in stable flows, FSI behaviour can lead to significant deviations in thrust and performance parameters. For more complex buzz flows, the effects of FSI behaviour on both the flowfield and structure remain unclear. In the authors' latest study (Ye, Zhou & Ye 2024), based on the variable-geometry lip of wide-speed-range scramjets, the FSI behaviour of the inlet is preliminarily studied. The results revealed that lip FSI could trigger buzz. During buzz, both violent and mild buzz modes coexist, alternating irregularly. This leads to intensified unsteadiness and nonlinearity in the flow, further deteriorating inlet performance. These studies demonstrate that inlet FSI behaviour significantly changes the flowfield structure and performance parameters, seriously affecting inlet start stability, inducing buzz, and modifying its characteristics.

According to the above studies, buzz is a self-sustained oscillatory flow with strong nonlinear and unsteady characteristics. It primarily occurs due to flow condition changes in rigid inlets – either at the entrance, such as variations in Mach number, angle of attack or capture area (Chang *et al.* 2012; Devaraj *et al.* 2021; Xu *et al.* 2022), or at the exit, such as variations in back pressure or throttling ratio (Tan, Sun & Yin 2009; Wagner *et al.* 2009; Huang *et al.* 2021). In the authors' recent study, it was confirmed that the flexible lip deformation can serve as a new buzz-inducing factor (Ye *et al.* 2024). Although the FSI behaviour of the flexible lip can trigger buzz, the resulting structural deformation alters the entrance flow, making it difficult to isolate FSI as the sole driver of instability. Furthermore, it should be noted that the flexible lip is essentially a specialised design derived from variable-geometry lips used in wide-speed-range scramjets, and thus lacks broader engineering applicability. Therefore, that case does not represent a typical FSI-induced instability process.

In sharp contrast, plate structures are widely used in hypersonic inlet design, yet their nonlinear dynamic behaviour under complex shocks has long been underestimated. Previous studies have shown that under shocks, the critical dynamic pressure of flexible plates decreases significantly (Visbal 2012; Ye & Ye 2018), their limit cycle oscillation amplitudes and frequencies are altered (Daub, Willems & Gülhan 2016; Boyer et al. 2018), and their nonlinear dynamic responses become increasingly complex (Brouwer et al. 2021; Ye et al. 2024). In some cases, the nonlinear dynamics of the plate can even promote flow transition, thereby causing changes in the flow structure (Shinde et al. 2018). Building on these findings, plate structures within inlets are prone to large-amplitude oscillations under shock loading, which can strongly interact with the internal flow and ultimately influence the buzz evolution. This interaction differs from flow condition changes at the inlet entrance or exit, and represents a new FSI-dominated mechanism for inducing flow instability. This raises several open questions. What is the specific mechanism by which plate FSI induces buzz? How does the buzz evolution under plate FSI differ from that in conventional rigid inlets or lip FSI inlets? What new characteristics does buzz exhibit under plate FSI? These questions remain unanswered.

Therefore, this study is the first to deeply reveal how a flexible plate induces inlet buzz through FSI, without relying on external flow condition changes. This finding holds significant academic and engineering value. It not only offers new insights into flow instability in hypersonic inlets but also provides theoretical support for inlet structural design and the development of instability control strategies.

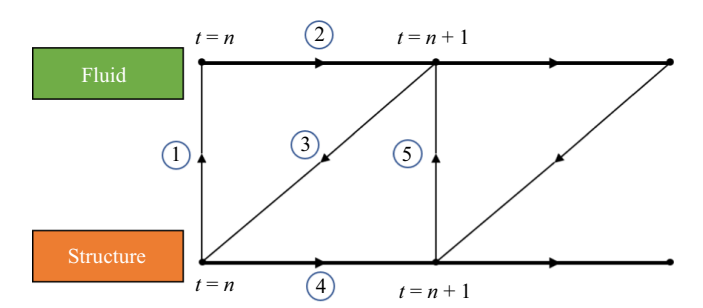


Figure 1. Flow chart for the loose coupling method.

The purpose of this study is to investigate the interaction process between buzz flow and a flexible plate, and to clarify the resulting changes in buzz characteristics. Hence this paper first establishes a high-order format method and verifies its reliability. Then the flow characteristics of a rigid inlet model are studied as a baseline. Finally, the buzz flow under FSI is analysed in detail.

2. Methodology and validation

This study employs an in-house computational fluid dynamics (CFD) code to solve the compressible Reynolds-averaged Navier–Stokes equation. The accuracy of the program has been verified in previous studies (Zha, Ye & Ye 2022; Hong, Ye & Ye 2023). In order to simulate the complex flowfield in the inlet, the $k-\omega$ shear stress transport model is adopted. The model has been used in many studies (Hong & Kim 2014; Shi *et al.* 2019), which can accurately capture shock structures and separation bubble structures. The above equations are solved using a finite difference method based on the cell-centred scheme (Liao, Ye & Zhang 2015). The left and right values of the primitive variables at the half nodes are obtained through the monotone upstream-centred scheme for conservation laws (MUSCL) with third-order accuracy. Subsequently, the convective fluxes at the half nodes are constructed using the van Leer method, while the viscous fluxes are calculated using a second-order central difference scheme (Liu *et al.* 2018; Shi *et al.* 2019). Time advancement is performed using the second-order implicit lower–upper symmetric Gauss–Seidel method (Liu *et al.* 2018).

Based on the finite element method (Brenner & Scott 2008), ANSYS is employed to compute the dynamic response of the plate (Ye *et al.* 2019). The governing equation can be written in the form

$$M\ddot{\xi} + G\dot{\xi} + (K_s + K_\sigma - K_a)\,\xi = U, \tag{2.1}$$

where M is the mass matrix, G is the damping matrix, K_s is the structural stiffness matrix, K_σ is the force stiffness matrix, and K_a is the initial load matrix; they are all $N \times N$ matrices. Here, U is the aerodynamic force matrix, which is an $N \times 1$ matrix obtained from CFD, and $\ddot{\xi}$, $\dot{\xi}$, $\dot{\xi}$ represent the acceleration, velocity and displacement of the structural motion, respectively.

The loose coupling method (Farhat & Lesoinne 2000) is adopted in this study to realise the two-way FSI, with the computational process shown in figure 1. The detailed description of this method and more comprehensive information on the CFD and Computational Structural Dynamics (CSD) methods can be found in our previous work (Ye *et al.* 2024).

The validation of the CFD numerical method and the CFD/CSD coupling computation has been completed and recognised in our previous work (Ye et al. 2024). The methods

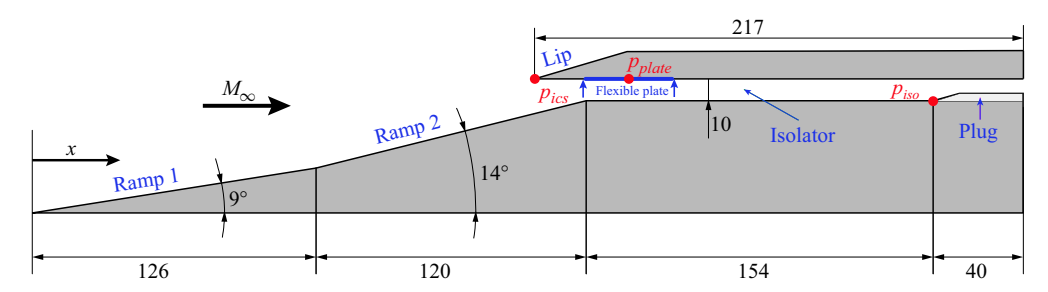


Figure 2. Two-dimensional inlet plate FSI model. (All dimensions are in mm.)

used in this study can accurately simulate both steady flowfields and unsteady buzz flowfields, and the fluid–structure coupling computation is also reliable.

3. Inlet plate FSI model

The calculation plate FSI model adopted in this study is a two-dimensional mixed-compression inlet proposed by Li *et al.* (2013). The geometric parameters of the rigid model are shown in figure 2. The internal contraction ratio is 1.53, and the total length of the model is 440 mm. There are two compression ramps at the entrance to compress the incoming flow. The first compression ramp is 126 mm long and has angle 9°; the second compression ramp is 120 mm long and has angle 14°. The internal height of the inlet is 10 mm. When the back pressure of the downstream combustor is too high, the inlet will buzz. The influence of downstream back pressure is simulated by setting a plug near the exit of the inlet. This method has been verified in numerical studies (Abedi, Askari & Soltani 2020; James, Suryan & Kim 2021). To quantify the degree of throttling, define the throttling ratio as

$$TR = 1 - \frac{A_{t,plug}}{A_{isolator}} = \frac{H_{plug}}{H_{isolator}},$$
(3.1)

where $A_{isolator}$ is the cross-sectional area of the isolator, $A_{t,plug}$ is the geometrical throat area at the plug, $H_{isolator}$ is the height of the isolator, and H_{plug} is the height of the plug.

The freestream conditions are consistent with the experiment of Li *et al.* (2013): Mach number 5.9, total pressure 1.27 MPa, total temperature 810 K, unit Reynolds number 5.2×10^{-6} m⁻¹.

For the plate FSI study, a flexible plate is set on the basis of the rigid inlet model, as indicated by the blue line in figure 2. The flexible plate is placed above the shoulder, affecting only the internal flow of the inlet. Since this region is located upstream within the inlet, the shock system is highly sensitive to structural deformation in this area, making it suitable for revealing the influence of plate FSI on flow characteristics. The plate has length 38.5 mm, thickness 5 mm, density 3500 kg m⁻³, Young's modulus set to 120 MPa, and Poisson's ratio 0.33. The finite element mesh of the plate is constructed using Shell63 and Surf154 elements for thin-plate structures. The two sides of the plate are simply supported, and deformation occurs only along the longitudinal axis. Modal analysis is performed using ANSYS APDL, yielding first natural frequency 273.9 Hz. Additionally, monitoring points, as shown in figure 2, are placed in three inlet regions: the internal compression section (p_{ics}), the flexible plate (p_{plate}) and the isolator (p_{iso}). The computational grid and boundary conditions are shown in figure 3, where the meshed area represents the fluid

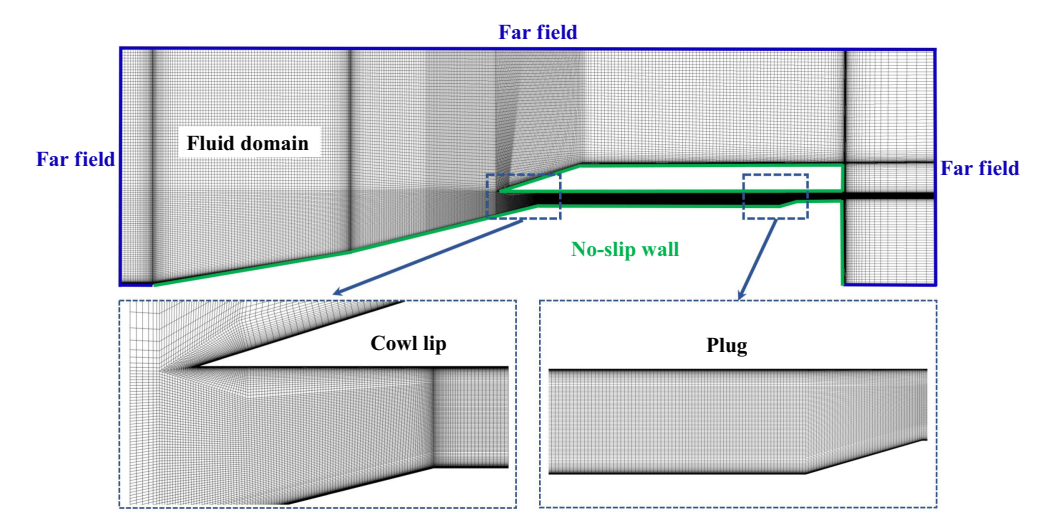


Figure 3. Computational grid and boundary conditions.

domain, the blue lines represent the far-field boundary, and the green lines represent the no-slip wall. Mesh convergence and time step sensitivity tests are provided in Appendix A.

4. Steady flow under the rigid plate

To establish a computational basis for the FSI simulation, this study first investigates the flow characteristics of the rigid inlet under different throttling ratios. The results show that buzz occurs when *TR* exceeds 34 %. To understand the initial flowfield characteristics, the steady flow structure prior to plate FSI is analysed.

The steady flowfield characteristics for TR = 32% and 34% are analysed. As the two conditions exhibit similar flowfield structures, figure 4(a) presents the pressure gradient distribution and local streamlines for TR = 32 %. Pressure gradient colouring is utilised to enhance the clarity of the shock/expansion wave structure (Liu et al. 2018; Ye et al. 2024). The lip shock impinges near the shoulder and reflects, interacting with the shock train at the plug. The upstream streamlines near the shoulder show that the interaction between the lip shock and the boundary layer causes boundary layer separation, which further induces the generation of expansion waves and a reattachment shock. The downstream streamlines reveal a large separation region at the plug. A strong oblique shock, induced by the separation region, interacts with the upper wall boundary layer, ultimately forming a distinct shock train structure at the plug (Ye et al. 2024). Figure 4(b,c) present the pressure distributions on the inlet walls for both conditions. The wall pressure remains consistent from the inlet entrance to x = 0.37 m. From x = 0.37 m to the inlet exit, the wall pressure distributions are similar for both conditions. However, for TR = 34%, the high-pressure region downstream of the shock train extends further, and the shock intensity near the plug is stronger. This behaviour has also been noted by Devaraj et al. (2020).

To better highlight the inducing effect of the plate FSI, an inlet with TR = 32% – still with a margin from the buzz onset – is selected as the simulation condition.

5. Buzz evolution under plate FSI

Previous analysis indicates that the flow within the rigid inlet at TR = 32% remains stable, exhibiting a typical steady flowfield. Building on this condition, the introduction of the

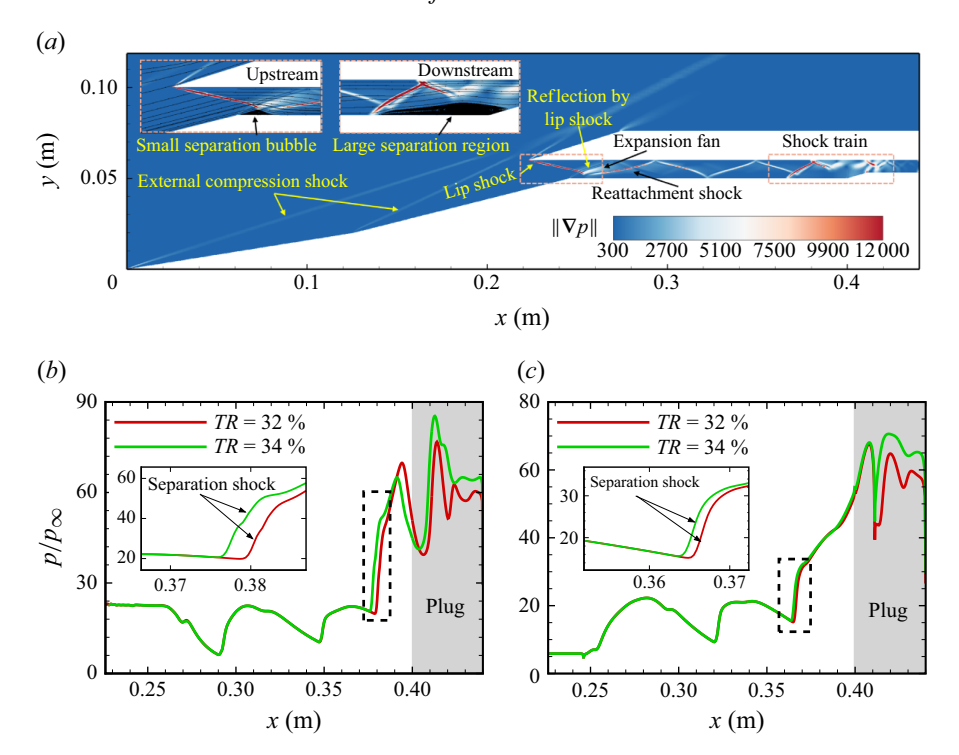
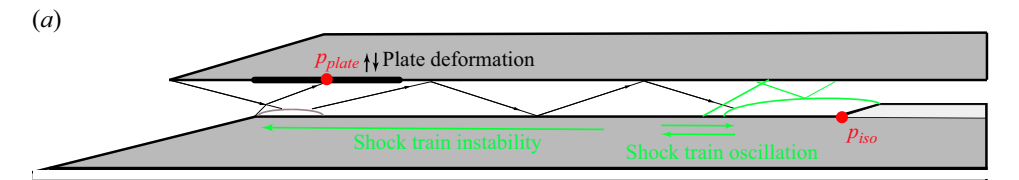


Figure 4. (a) Pressure gradient distribution for steady flow under TR = 32%. Wall pressure distributions on (b) the lip side and (c) the ramp side for TR = 32% and 34%.

flexible plate initiates plate FSI, which gradually drives the originally stable flow to evolve towards instability.

5.1. Gradual-onset buzz induced by plate FSI

Figure 5(a) illustrates the shock structure of the steady flow at TR = 32% (as described in § 4). Additionally, it schematically indicates the dynamic response of the flexible plate (black arrows) and the motion of the shock train (green arrows) before buzz under FSI. At the initial moment, the separation shock at the shoulder impinges on the flexible plate. Under the influence of this shock, the plate begins to oscillate slightly, initiating FSI. Figure 5(b) presents the time history of the midpoint displacement of the plate, while figure 5(c) shows the pressure pulsation at the plug (p_{iso}) . In the supersonic flow within the inlet, the plate's dynamic response leads to downstream pressure oscillations. The downstream pressure partially reflects the shock train's position (Xiong et al. 2018). Results show that once FSI is introduced, the plate undergoes slight oscillations with gradually increasing amplitude. Simultaneously, the downstream pressure begins to oscillate synchronously, indicating that the shock train performs periodic upstreamdownstream motion along the wall. Subsequently, the plate displacement shows a sharp rise at a certain moment, while the downstream pressure suddenly increases followed by a rapid drop. This indicates shock train instability and its expulsion from the inlet. Finally, the onset of buzz is characterised by violent plate oscillations and large-amplitude pressure pulsations. These results clearly demonstrate that plate FSI can destabilise the flow and trigger buzz. This raises an important question: how does the buzz evolution under plate FSI differ from that in conventional rigid or lip FSI inlets?



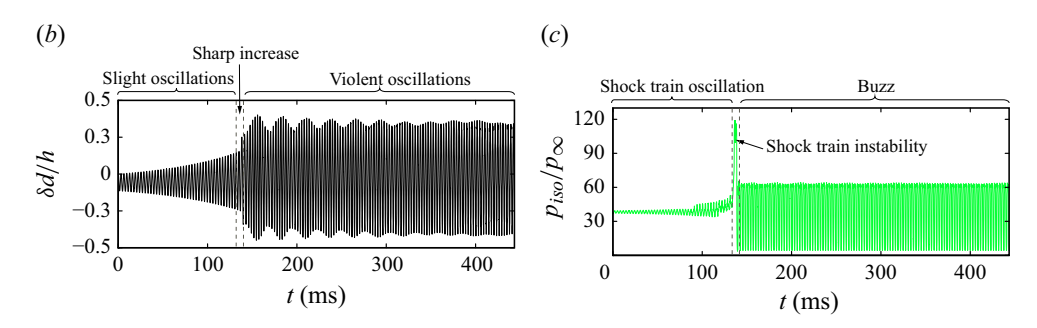


Figure 5. (a) Schematic of the internal shock structure and plate/shock train responses under FSI. Time histories of (b) plate displacement and (c) pressure pulsation at the plug.

In previous studies, inlet buzz typically occurs under extreme flow conditions such as high angles of attack and large throttling ratios (Tan et al. 2009; Wagner et al. 2009; Xu et al. 2022). Under these conditions, rigid inlets experience rapid buzz evolution. Consequently, there has been little research focused on the detailed evolution of the flow instability. Figure 6 compares the time histories of pressure pulsations at the downstream plug among three cases: rigid inlet buzz, lip FSI buzz (Ye et al. 2024) and plate FSI buzz. The results show that the buzz evolution in rigid inlets typically includes a transition stage and a buzz stage, with instability developing within just one or two buzz cycles in figure 6(a). In this study, such rapidly developing instability is referred to as 'abrupt-onset' buzz, which is consistent with the general buzz in previous studies (Wagner et al. 2009; Tan et al. 2011). In the lip FSI buzz, the deformation of the lip structure alters the inlet geometry and thereby modifies the incoming flow. As a result, the flow also becomes unstable within one or two buzz cycles in figure 6(b), exhibiting the same abrupt-onset characteristic. In contrast, the plate FSI buzz exhibits a fundamentally different 'gradualonset' characteristic. In figure 6(c), in addition to the transition and buzz stages, the process includes a clearly identifiable instability accumulation process. During this process, the pressure pulsations develop gradually, and the total evolution time of instability extends to more than 20 times that of the abrupt-onset buzz. Admittedly, previous studies have simulated similar gradual-onset behaviour by gradually varying the angle of attack or blockage ratio (Xu et al. 2017; Xiong et al. 2018). However, unlike these externally driven mechanisms, the gradual-onset instability identified in this study is caused by the selfexcited effects under FSI. It represents a more physically general path to buzz. How, then, does the plate FSI induce buzz through this instability accumulation process? This mechanism warrants further investigation.

In light of the differences between the gradual-onset buzz investigated in this study and conventional abrupt-onset buzz, the evolution of the former can be divided into two primary processes: a unique instability accumulation process, and a subsequent complete instability process, which resembles that of the abrupt-onset buzz.

According to the characteristics of pressure pulsations and the evolution of the flowfield structures, the instability accumulation process can be further subdivided into two stages.

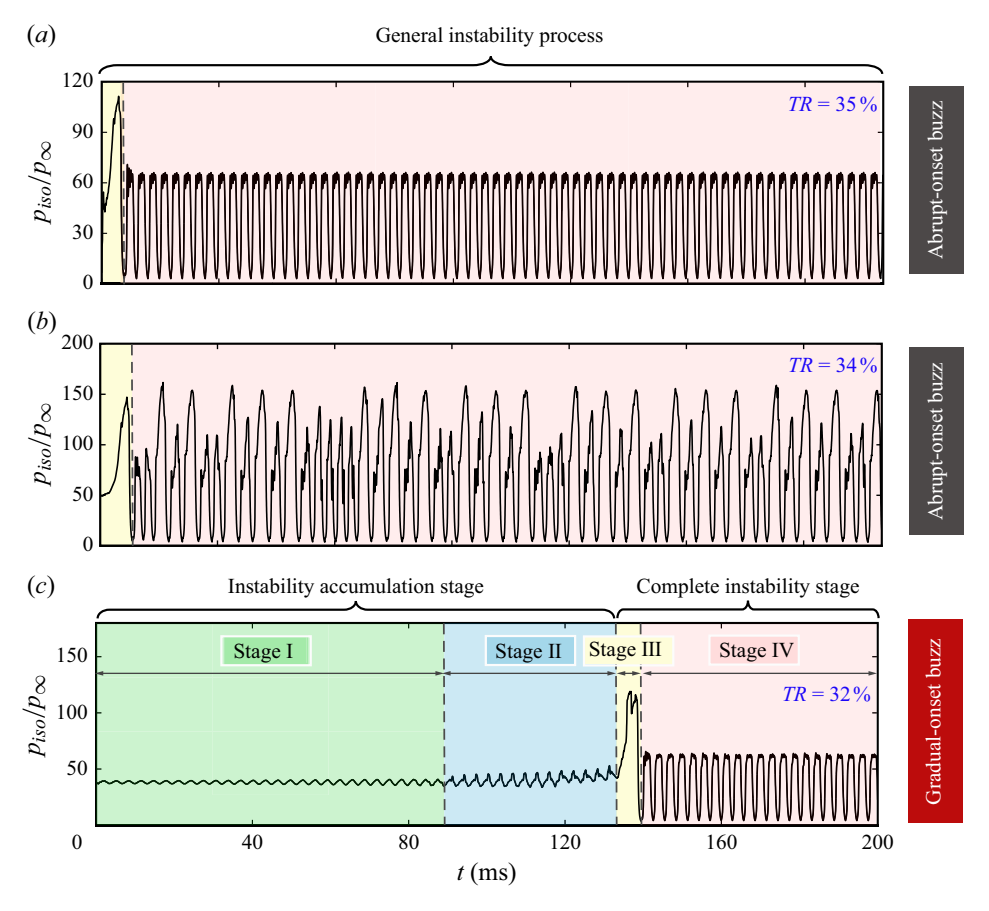


Figure 6. Time histories of pressure pulsations at the downstream plug among three cases: (a) rigid inlet buzz, (b) lip FSI buzz (Ye et al. 2024), and (c) plate FSI buzz.

- (i) Linear development stage (stage I): the displacement amplitude of the plate gradually increases, while the pressure pulsation amplitude at the plug exhibits a slow, linear growth trend.
- (ii) Nonlinear development stage (stage II): the plate displacement continues to increase, and the pressure pulsation amplitude displays a nonlinear growth trend. Upon entering the complete instability process, the flow evolution proceeds through the following two stages.
- (iii) Transition stage (stage III): the plate displacement amplitude rises sharply, accompanied by a rapid increase in pressure.
- (iv) Buzz stage (stage IV): both the pressure and the plate displacement exhibit strong, periodic oscillations.

Therefore, the gradual-onset buzz evolution induced by plate FSI clearly exhibits a multistage characteristic.

5.2. Multistage flow evolution of gradual-onset buzz

To clearly investigate the instability evolution characteristics at each stage of the flowfield, this study examines each stage in terms of plate displacement, pressure pulsations and

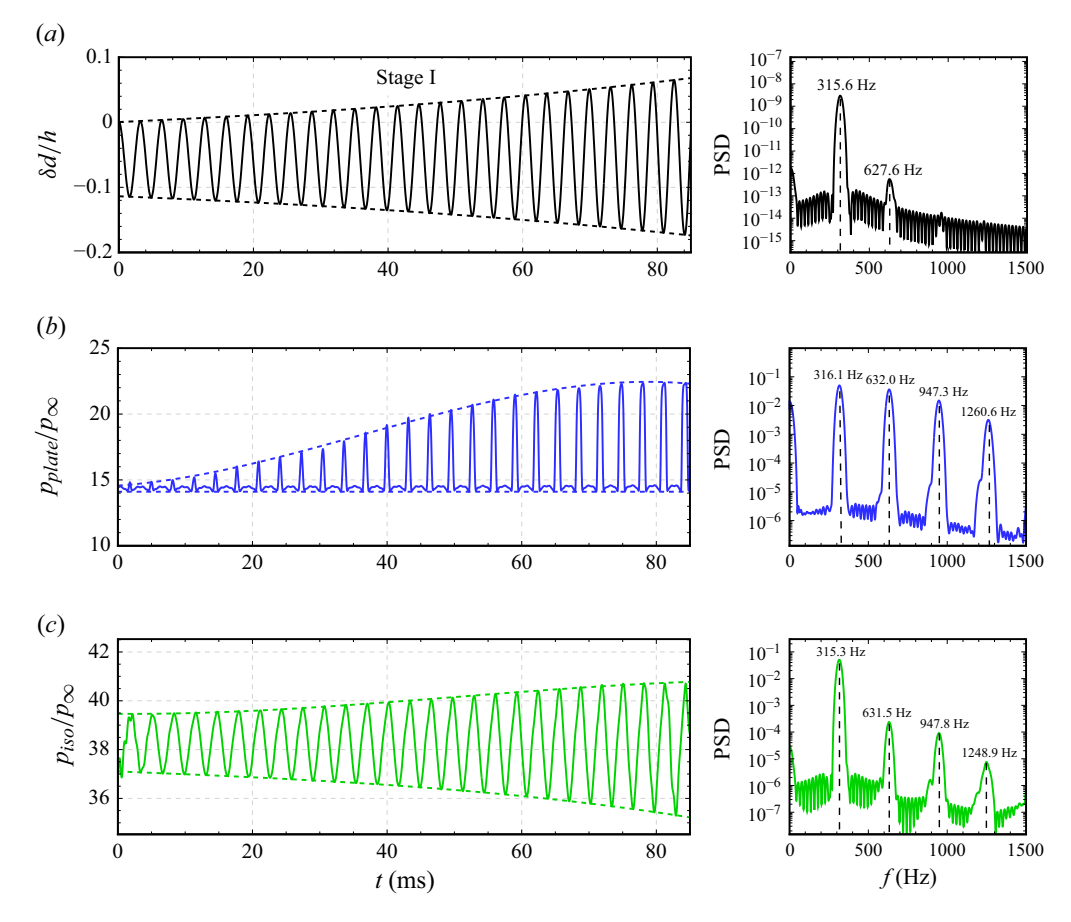


Figure 7. Time histories and PSDs of plate displacement and pressure pulsations at stage I.

flowfield structure, aiming to reveal the core mechanisms underlying the overall instability evolution.

5.2.1. Instability accumulation process driven by plate FSI

When FSI begins, the flexible plate undergoes slight periodic oscillations under the influence of shocks. These oscillations induce corresponding fluctuations in the downstream flow. As the oscillation amplitude progressively increases, the downstream flowfield becomes increasingly unstable. During this process, the plate's dynamic response plays a dominant role in driving the instability.

(i) Linear development stage (stage I). Under the influence of the separation shock at the shoulder, the plate begins to exhibit slight oscillations in its first natural mode. The plate's oscillations induce corresponding oscillations in the downstream flowfield structure. The FSI enters stage I. Figure 7(a) shows the time history and power spectral density (PSD) of the plate displacement (d_{plate}), while figure 7(b,c) show these of pressure pulsations (p_{plate} , p_{iso}) in different regions (p_{ics} is a constant value, not shown). Dashed lines indicate the envelope of the signals, clarifying the amplitude variation over time. Both the amplitudes of the plate displacement and pressure pulsations exhibit a slow linear growth trend. In the frequency domain, the dominant frequencies of pressure pulsations at the plug (p_{iso}) and the plate (p_{plate}) are approximately 315 Hz, consistent with the dominant frequency

of the plate displacement (d_{plate}). This value is higher than the first natural frequency 273.9 Hz reported in § 3. This discrepancy arises because the unsteady aerodynamic loading introduces geometric nonlinearities and effectively increases the stiffness of the plate, resulting in a higher response frequency under FSI. As the plate is located upstream of the flowfield, the unsteady oscillation characteristic of the flow is dominated by the plate displacement at this stage. Additionally, the frequency of the plate displacement is relatively simple, while there are many harmonic components in the pressure pulsations oscillation frequencies.

Figure 8 shows the pressure gradient distributions of flowfield and plate deformation at stage I. In order to show the plate deformation clearly, the inlet structure is shown in grey, with the enlarged plate deformation marked on the left-hand side. From moments (1)–(3), the plate exhibits convex downward deformation, narrowing the isolator flow, and forming an increasing oblique shock at the leading edge of the plate. This oblique shock interacts with the lower wall boundary layer, causing the separation bubble at the shoulder to expand. The increased separation bubble not only strengthens the separation shock at the shoulder, but also increases the reflection angle of the reflected shocks. The increased reflection angle causes the background shock system to shift upstream. Since the large separation bubble ahead of the plug is formed by the combined influence of the reflected shock and the shock train, the upstream movement of the reflected shock leads to an upstream shift of the adverse pressure gradient that it imposes on the boundary layer. This upstream shift of the adverse pressure gradient region, in turn, drives the shock train to move upstream as well. From moments (3)–(5), the plate deformation decreases, weakening the plate oblique shock and the separation shock at the shoulder. The reflected shocks drive the shock train downstream. From moments (5)–(7), the plate exhibits concave upward deformation, widening the isolator flow and generating expansion waves at its leading edge. These expansion waves interact with the lower wall boundary layer, weakening the oblique shock at the shoulder. However, due to the weakness of the expansion waves, the separation bubble at the shoulder exhibits no significant change. The reflected shocks and shock train continue to move downstream. From moments (7)–(9), the plate deformation decreases, weakening the plate expansion waves. The reflected shocks move upstream. However, the shock train continues to move downstream from moments (7)–(8), and only begins to reverse upstream between moments (8) and (9). This hysteresis is present throughout the oscillatory cycle, but becomes particularly evident during moments (7)–(9) due to the relatively short sampling interval associated with the plate's upward deformation.

In each cycle of stage I, the slight oscillation of the plate causes minor oscillations of the upstream reflected shocks and the downstream shock train. Accompanying the plate deformation, the movement of the shock train's foot near the plug exhibits a smooth and regular oscillation, as shown by the black dashed line.

(ii) Nonlinear development stage (stage II). The intensification of plate oscillation enlarges the oscillation range of internal shock structures, especially the shock train. When the shock train interacts with or separates from the reflected shock foot, the shape changes. The FSI enters stage II. Figure 9 shows the time histories and PSDs of the plate displacement (d_{plate}) and pressure pulsations (p_{plate} , p_{iso}) at stage II. Compared to stage I, the amplitude of the plate displacement continues to exhibit a slow linear growth trend. However, the amplitudes of pressure pulsations show a nonlinear growth trend with evident small-amplitude high-frequency oscillations. At the midpoint of the plate, the amplitude of pressure pulsation (p_{plate}) varies slightly, while the high-frequency pulsations gradually strengthen. At the plug, the amplitude of pressure pulsation (p_{iso}) exhibits a significant nonlinear growth trend. In the frequency domain, the dominant frequency of pressure pulsation at the midpoint of the plate (p_{plate}) is approximately 322.5 Hz, which

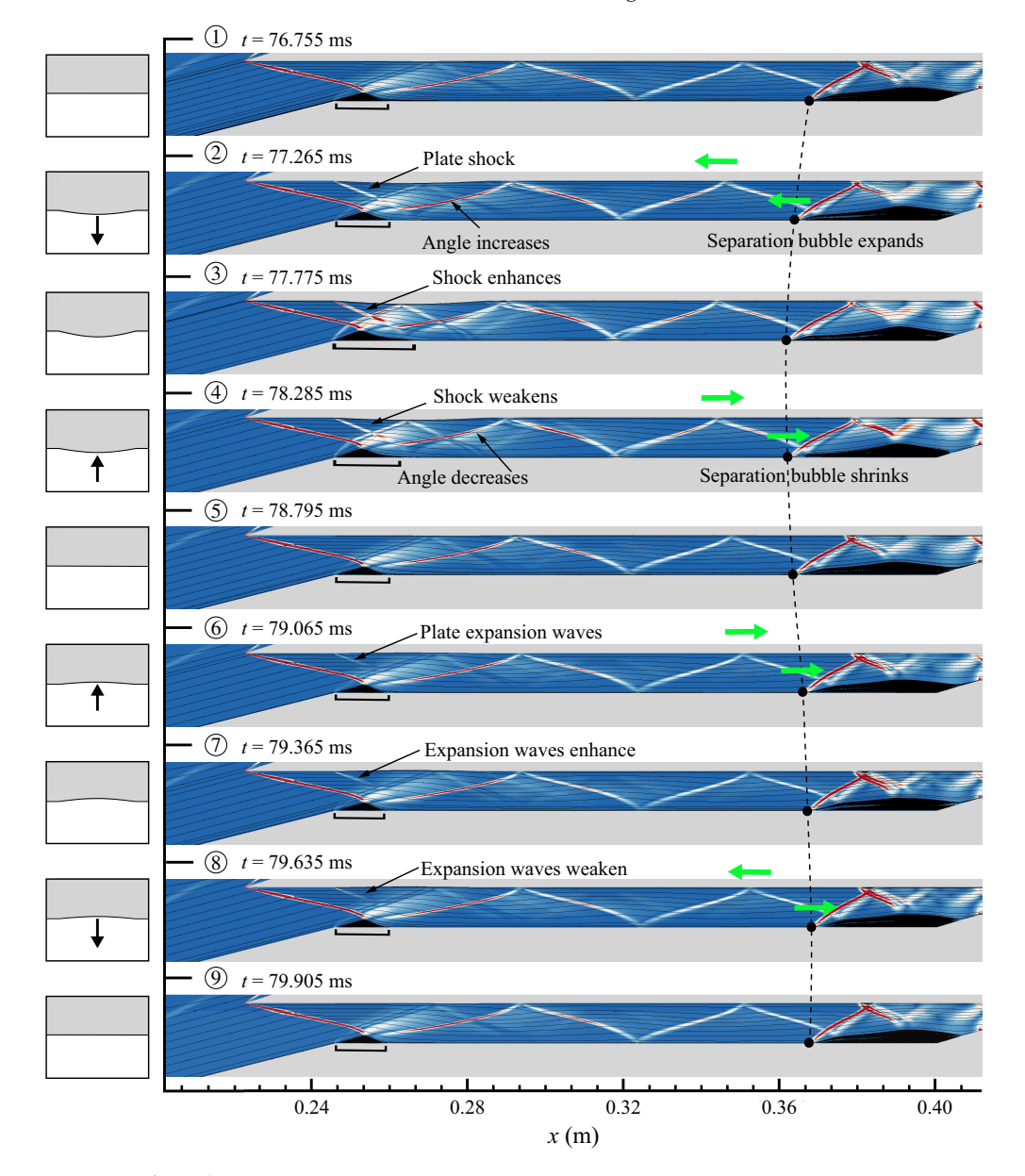


Figure 8. Pressure gradient distributions of flowfield and plate deformation at stage I.

is consistent with that of the plate displacement (d_{plate}). Due to the influence of small-amplitude high-frequency oscillations, the main frequency of the pressure pulsation at the plug (p_{iso}) is 317.6 Hz, which is slightly less than 322.5 Hz. Compared with figure 7, p_{iso} in stage II shows significantly more non-harmonic features. Overall, oscillation of the flowfield structures within the inlet is still dominated by this plate, and the oscillation frequency has slightly increased compared to stage I.

Similar to stage I, transient flowfields at nine selected moments are analysed. Figure 10 shows the pressure gradient distributions of the flowfield and plate deformation at stage II. From moments (1)–(3), the plate exhibits convex downward deformation. As the plate

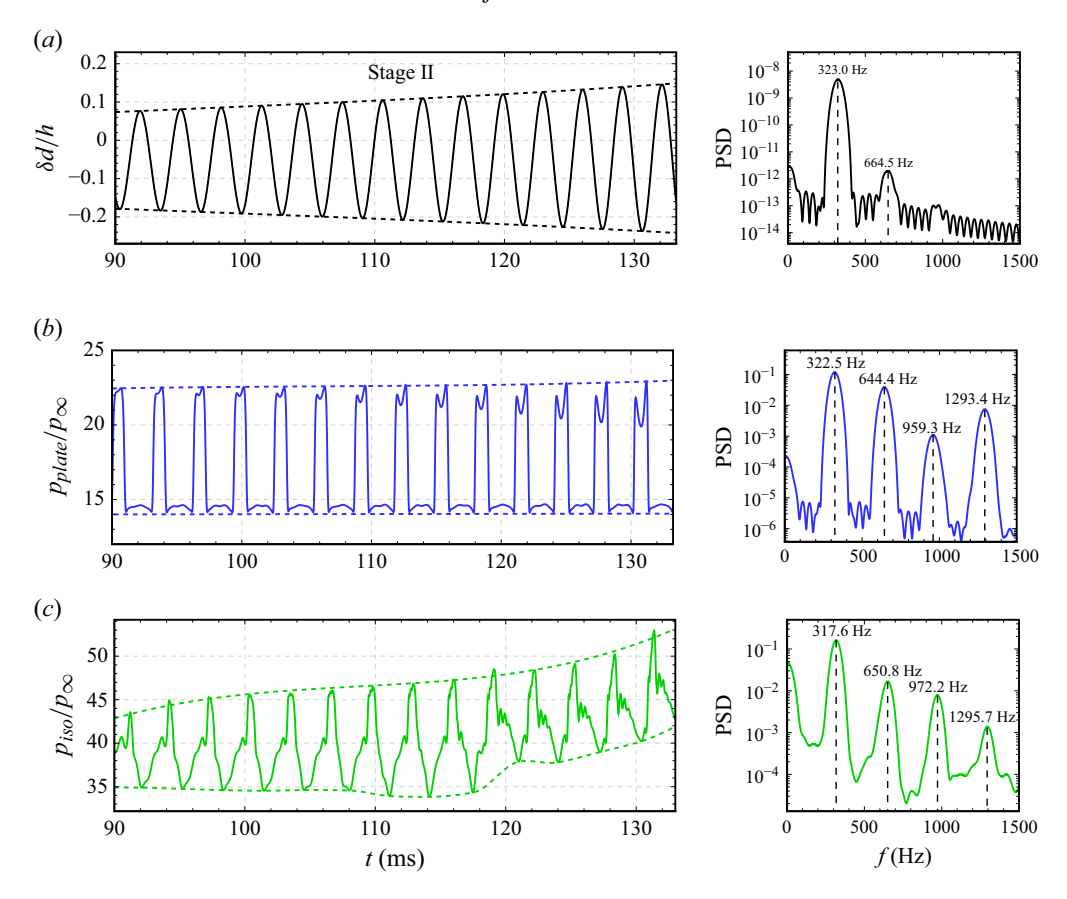


Figure 9. Time histories and PSDs of plate displacement and pressure pulsations at stage II.

deformation increases, the reflected shock wave moves upstream, thereby inducing the upstream movement of the shock train. At moment (4), when the reflected shock reaches its most upstream position, the downstream separation region expands, but the leading edge of the separation bubble becomes significantly thinner. This indicates that the adverse pressure gradient generated by the reflected shock acting on the boundary layer is notably weakened. From moments (4)–(5), the reflected shock can no longer sustain a sufficient adverse pressure gradient to hold the shock train upstream, causing the shock train to shift downstream and separate from the reflected shock foot on the lower wall. After the separation, the adverse pressure gradient continues to decrease, leading to a rapid downstream movement of the shock train. Meanwhile, the interaction between the reflected shock foot on the upper wall and the shock train increases the adverse pressure gradient, inducing flow separation and an oblique shock on the upper wall. The shape of the shock train transforms from asymmetric to symmetric. At moment (6), the plate exhibits concave upward deformation, and expansion waves are induced. The reflected shocks move downstream. The interaction between the reflected shock foot on the lower wall and the shock train causes the shock train to move upstream. The shock train returns to an asymmetric shape. From moments (7)–(9), the plate deformation decreases, weakening the plate expansion waves. The changes of the internal shock system are similar to those of stage I.

In each cycle of the stage II, due to the further increase in the amplitude of plate displacement, the oscillation of upstream reflected shocks and the downstream shock train

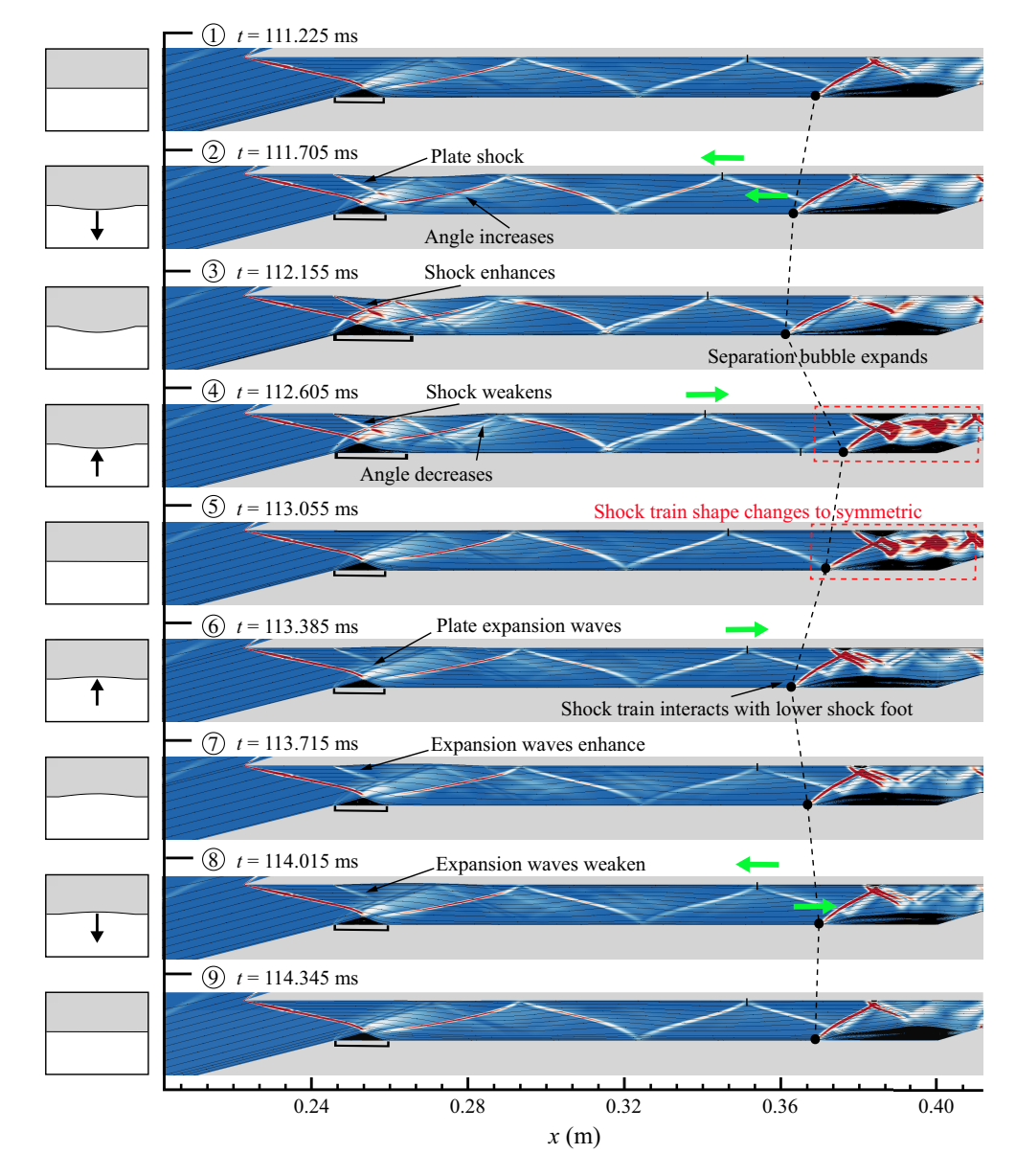


Figure 10. Pressure gradient distributions of flowfield and plate deformation at stage II.

intensifies. Accompanying the plate deformation, the movement of the shock train's foot near the plug exhibits irregular changes, as shown by the black dashed line.

Overall, during the instability accumulation process, the plate FSI drives the development of flow instability within the inlet. Under FSI, the plate oscillation governs the motion of the downstream shock train by altering the background shock system. As the amplitude of the plate oscillation increases, the shock train oscillation is also intensified. When the shock train oscillates excessively, the interaction between the feet of the reflected shocks and the shock train alternates between the upper and lower walls, resulting in a significant change in the shock train shape during its oscillatory motion. Consequently,

the originally smooth and regular oscillation evolves into irregular behaviour, markedly increasing the downstream instability.

As the FSI effect continues, the system gradually approaches a critical instability threshold. Although the plate displacement is still within the small amplitude, the local disturbances that it induces lead to a continuous increase in the unsteadiness of the downstream flowfield. This instability accumulation process lays a crucial foundation for the eventual breakdown of flow stability.

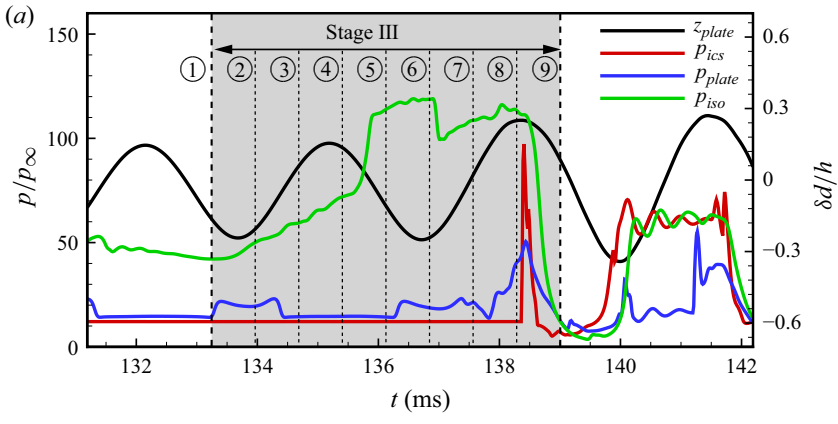
5.2.2. Buzz-dominated complete instability process

Once the instability surpasses the critical threshold, the flowfield evolution then enters the complete instability process, dominated by buzz. During this process, although the plate FSI still participates in the flow evolution through two-way coupling, the strongly nonlinear dynamic characteristics of the buzz phenomenon dominate the overall flowfield evolution.

(iii) Transition stage (stage III). As the oscillation amplitude of the plate continues to increase, the pressure in the downstream high-pressure region rises continuously, eventually reaching a critical point. Then the high-pressure region begins to move rapidly upstream, and the FSI enters stage III. Figure 11(a) shows the plate displacement and pressure pulsations at stage III. The pressure at the plug (p_{iso}) increases steadily for a period before reaching its peak, while the pressures at the midpoint of the plate (p_{plate}) and at the lip (p_{ics}) rapidly increase to their peaks. Subsequently, pressure pulsations at all three monitoring points $(p_{iso}, p_{plate}, p_{ics})$ exhibit significant oscillations. Based on the analysis of pressure pulsations for the rigid inlet, it can be inferred that at this stage, the FSI has induced flow instability, leading to the occurrence of buzz. Moreover, the large amplitudes of pressure pulsations induced by buzz further contribute to the rapid increase in the amplitude of the plate displacement.

Unlike stages I and II, the flowfield develops rapidly in a short period of time at stage III. Nine time-averaged transient flowfields are selected for analysis, as shown in figure 11(a). Figure 11(b) shows the pressure gradient distributions of the flowfield and the plate deformation at stage III. From moments (1)–(2), the plate exhibits a convex downward deformation, generating an increasing oblique shock, expanding the separation bubble at the shoulder. Simultaneously, the downstream shock train begins to move upstream due to the increasing pressure at the plug (p_{iso}) . At moment (3), the plate exhibits a concave upward deformation, inducing the expansion waves. As the shock train moves upstream, it interacts with the reflected shock foot on the upper wall, inducing an oblique shock, which changes the shape of the shock train from asymmetric to symmetric. From moments (4)–(5), the plate exhibits a convex downward deformation again, and the expansion waves transform into an oblique shock. The high pressure at the plug (p_{iso}) accelerates the upstream movement of the shock train. During this movement, the oblique shock on the upper wall interacts with the reflected shock. The increased adverse pressure gradient induces the flow separation to develop rapidly upstream, resulting in an upstream jump of the oblique shock. This jumping characteristic is similar to the observations made by Xu et al. (2017). From moments 6–7, the shock train first interacts with the shock foot on the lower wall and deflects to the top surface. It then interacts with the shock foot on the upper wall and deflects to the bottom surface, expanding the separation bubble at the shoulder. At moment (8), the shock train arrives at the shoulder and pushes the ramp separation shock upstream. As the shock train passes, there is a sharp increase in pressure at the plate (p_{plate}) and the lip (p_{ics}) . Meanwhile, the plate displacement is also significantly increased by the excitation of the flow. At moment (9), the internal pressure

K. Ye, Y. Guo, X. Zhou, H. Zhang and Z. Ye



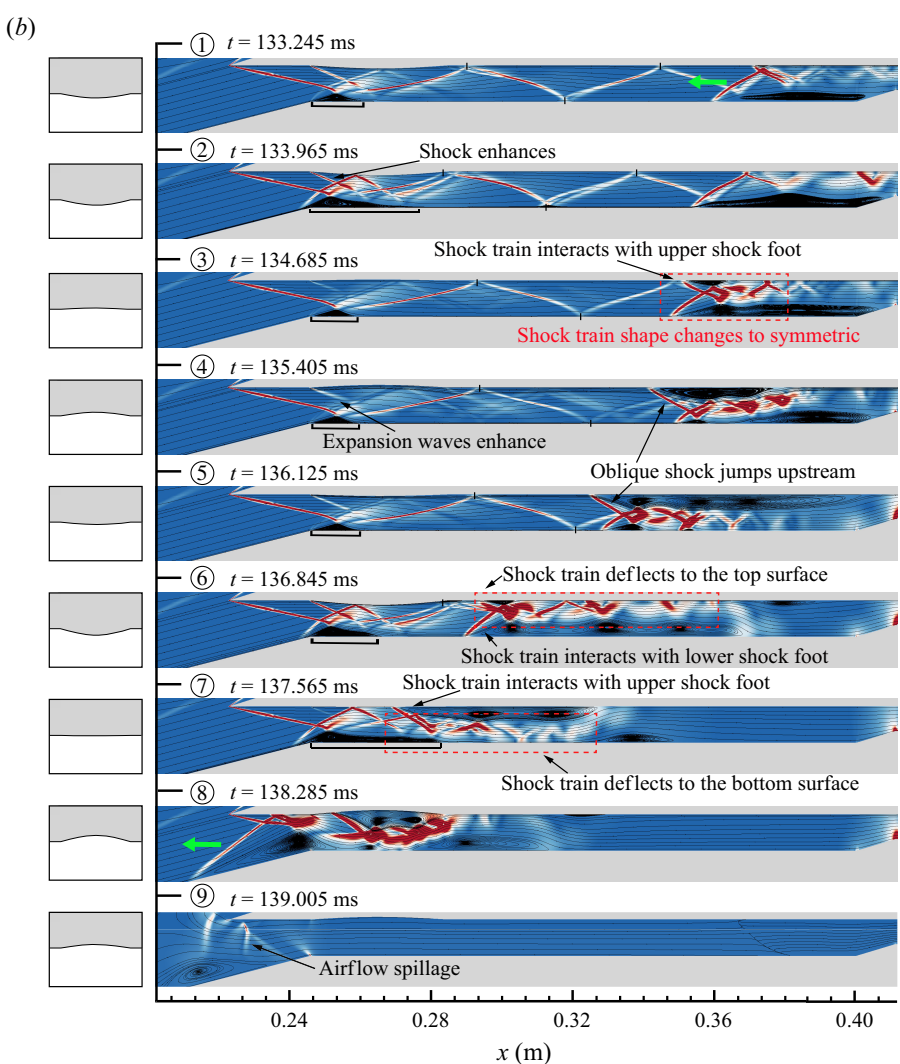


Figure 11. (a) Plate displacement and pressure pulsations for nine moments. (b) Pressure gradient distributions of flowfield and plate deformation at stage III.

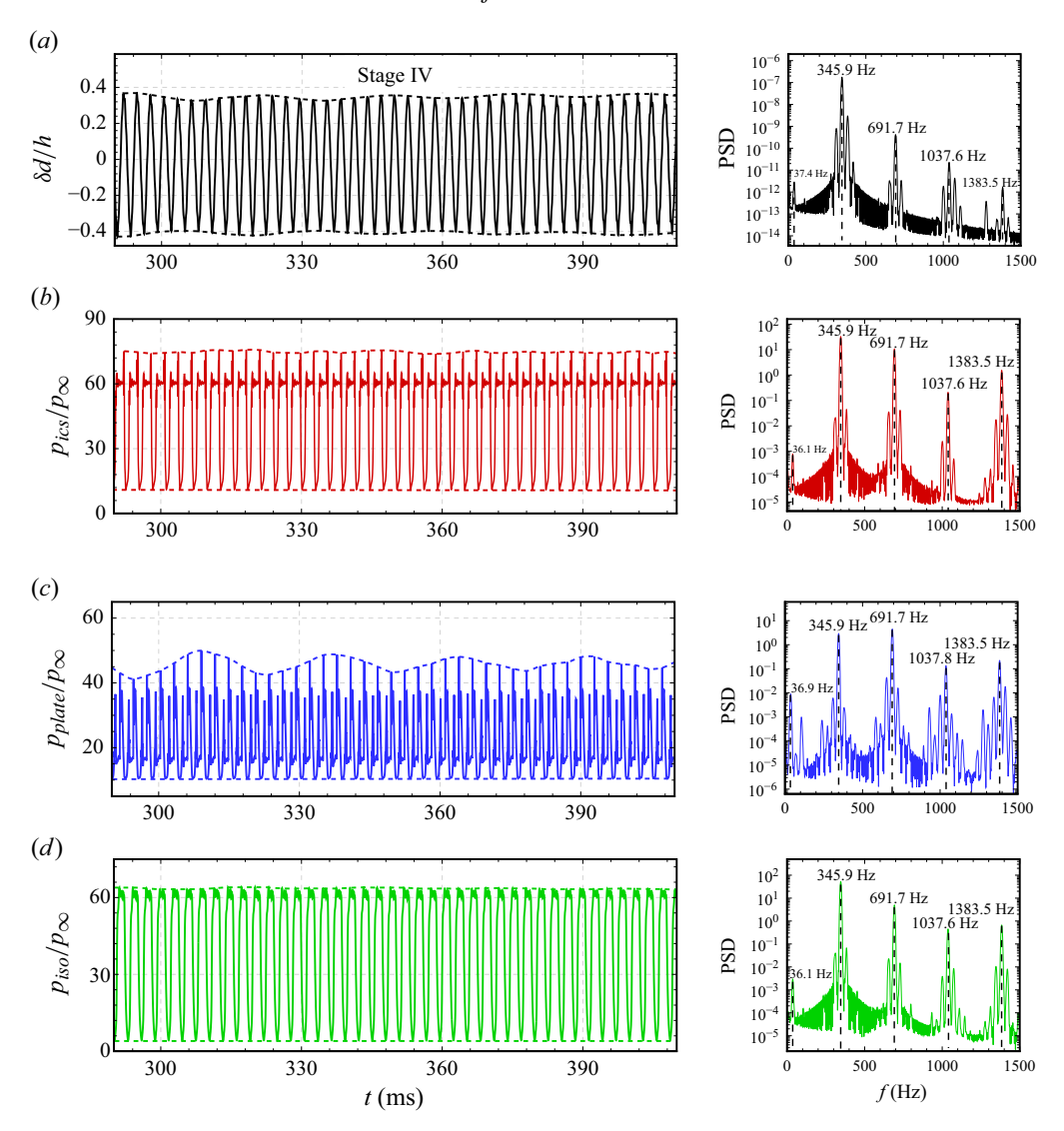


Figure 12. Time histories and PSDs of plate displacement and pressure pulsations at stage IV.

 $(p_{iso}, p_{plate}, p_{ics})$ is released, and the airflow spillage occurs. The ramp separation shock moves downstream, marking the end of the transition stage.

(iv) Buzz stage (stage IV). After the shock train is pushed out of the inlet, buzz occurs. Figure 12 illustrates the time histories and PSDs of the plate displacement and pressure pulsations at stage IV. Both the plate displacement (d_{plate}) and pressure pulsations (p_{iso} , p_{plate} , p_{ics}) exhibit significant oscillations, indicating the occurrence of buzz. Similar to the pressure pulsations of buzz within the rigid model, those within the flexible plate model also have small-amplitude high-frequency oscillations. Meanwhile, in figure 12(a,c), the envelopes of the plate displacement and pressure pulsations exhibit a distinct pattern of periodic waxing and waning, indicating that the interaction between the plate vibration and buzz flow gives rise to a 'beating' phenomenon. In the frequency domain, the dominant and harmonic frequencies of the plate displacement (d_{plate}) match precisely with those of the pressure pulsations (p_{iso} , p_{plate} , p_{ics}). The main frequency is 345 Hz, which is slightly

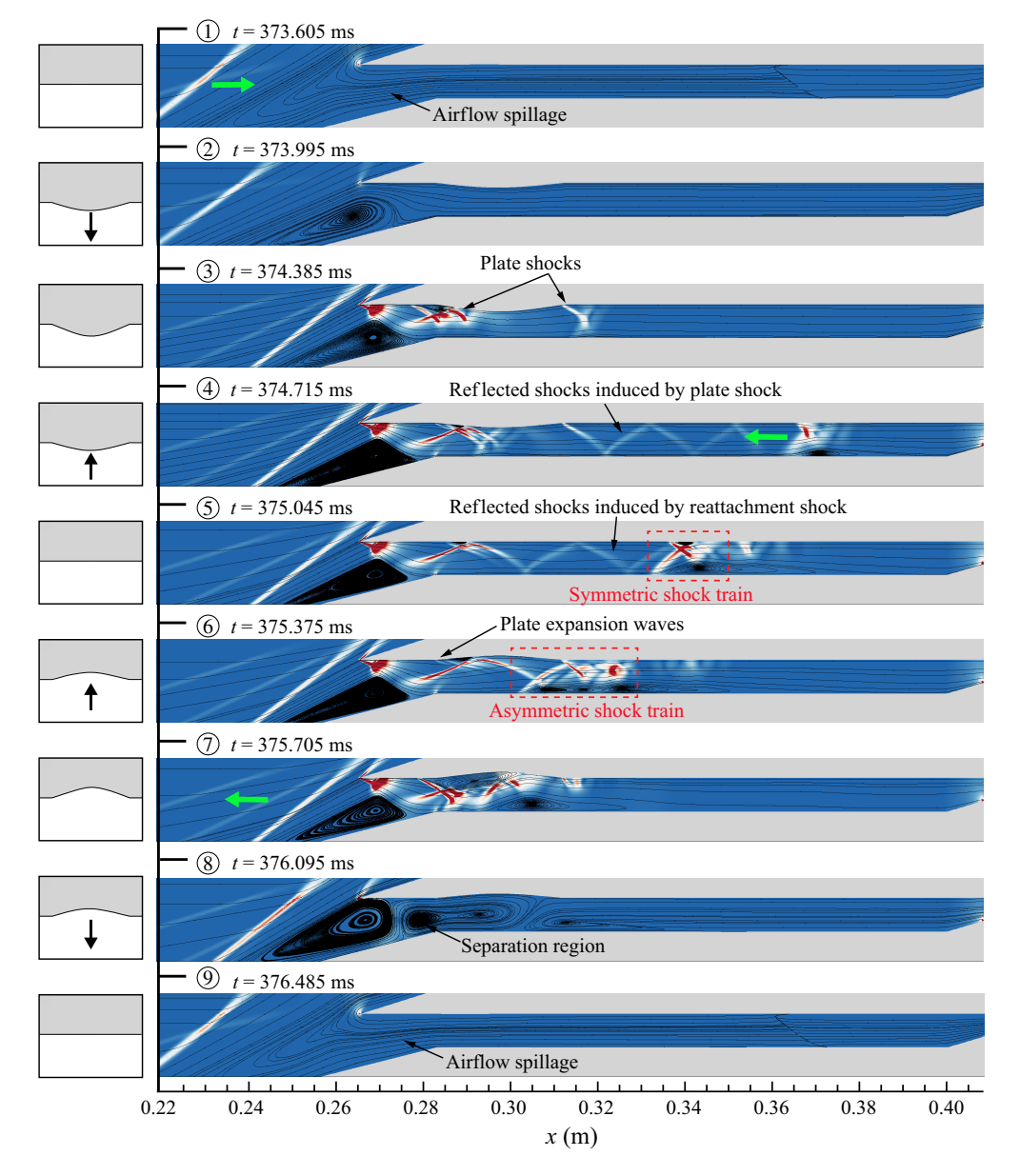


Figure 13. Pressure gradient distributions of flowfield and plate deformation at stage IV.

higher than that at stage II. Both the plate displacement and pressure pulsations have a low-frequency component of approximately 37.4 Hz. This frequency corresponds to the 'beating' phenomenon generated by FSI. The interaction between the dynamic response of the plate and buzz flow achieves dynamic stability.

Similar to the analyses conducted at stages I and II, nine transient flowfields are selected based on the plate displacement. Figure 13 illustrates the pressure gradient distributions and plate deformation. From moments 1—2, the ramp separation shock is distant from the lip, and airflow spillage occurs near the lip. Furthermore, no shock structure is present within the isolator, indicating that the flow is subsonic. At moment 3, the plate reaches its maximum convexity, inducing two oblique shocks at the leading and trailing edges of the

plate. The ramp separation shock moves downstream towards the lip, and a strong lip shock forms. At moment ④, the reflected shocks induced by the plate oblique shock propagate downstream. Simultaneously, the downstream high-pressure region drives a shock train moving upstream. From moments ⑤—⑥, the oblique shocks induced by plate deformation disappear. At this time, the reflected shocks are induced by the reattachment shock. Due to the interaction between the shock train and the shock feet, the shock train's initially symmetric structure becomes asymmetric. At moment ⑦, the downstream shock train moves to the shoulder, engulfing the reflected shocks. As the plate exhibits a concave upward deformation, a large separation bubble is triggered on the upper wall. The shock train deflects to the bottom surface, and the three separation bubbles on the lower wall are merged into one. From moments ⑧—⑨, the shock train pushes the ramp separation shock upstream, resulting in airflow spillage. The shock structures within the isolator disappear, indicating that the flow returns to subsonic.

Overall, during the complete instability process, the unsteady nature of buzz itself dominates the oscillation of the flowfield. When the downstream pressure peaks, the shock train becomes unstable and gradually propagates upstream (Wagner *et al.* 2009; Zhang *et al.* 2016*a,b*). During this upstream motion, the shock train interacts with the reflected shocks, leading to a significant change of its shape, consistent with the observations of Shi *et al.* (2019). As the shock train sweeps across the plate, the plate displacement rises sharply. Subsequently, buzz occurs. The strong nonlinear and unsteady characteristics inherent to the buzz dominate the oscillation of the flowfield and induce intense oscillation of the plate. Ultimately, the interaction between the dynamic response of the plate and the buzz flow reaches a dynamically stable state.

5.3. Energy instability mechanism in gradual-onset buzz

As shown in the previous subsection, under plate FSI, the inlet flowfield undergoes a significant multistage evolution, ultimately developing into a stable periodic buzz state. To explore the underlying causes of this gradual-onset buzz, the dynamic mode decomposition (DMD) method (Schmid 2010) is used to analyse the unstable characteristics of the four stages and reveal the mechanism of unstable energy. The DMD method can decompose obtained modes into individual frequencies and growth rates, directly characterising flow evolution through singular modes and eigenvalues. It has also been applied to the analysis of flow instability in previous studies (Rowley & Dawson 2017; Zha *et al.* 2022).

Based on the plate displacement, five cycles are selected for analysis at each stage, with approximately 500 transient flowfields chosen. The analysed physical quantity is the pressure gradient. In figure 14, the real and imaginary parts of the eigenvalues are plotted after taking the logarithm. The black points represent convergent or stable modes with negative growth rates, and red points represent unstable modes with positive growth rates. The distributions of unstable modes at stages I and II are quite similar, with most growth rates being less than 50. Only two modes have growth rates slightly above 50, indicating that most modes exhibit a weakly divergent tendency. At stage III, the growth rates of unstable modes increase. Among them, 26 modes have growth rates exceeding 50, with the maximum reaching 107, indicating significantly enhanced instability. At stage IV, the number of unstable modes significantly decreases. All growth rates of unstable modes are less than 50, exhibiting a weakly divergent tendency.

To measure the contribution of each mode to the whole dataset, we define the energy of each mode as (Zha *et al.* 2022)

$$E_i = \sum_{j=1}^{N} |c_{ij}| \| \boldsymbol{\phi}_i \|_2, \tag{5.1}$$

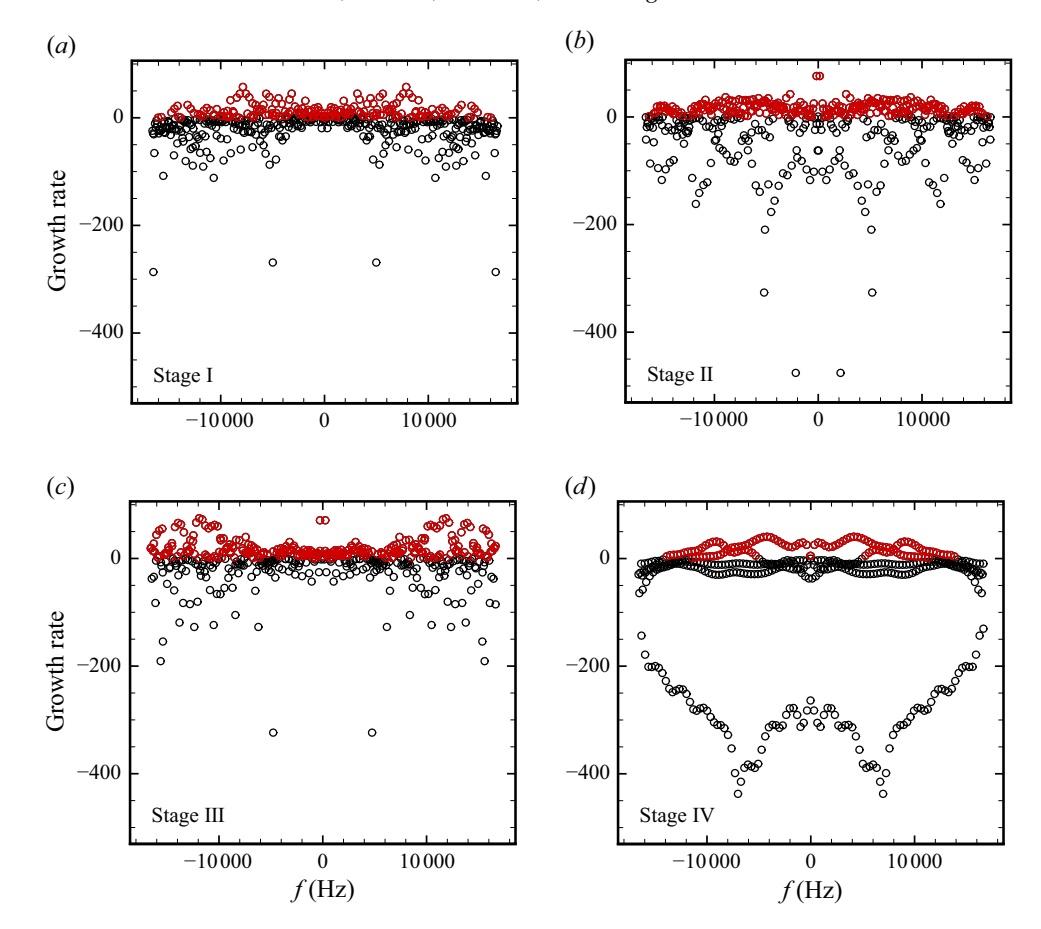


Figure 14. Distributions of real and imaginary parts of the logarithmic eigenvalues.

where ϕ_i represents the *i*th order DMD mode, c_{ij} represents the mode coefficient of the *i*th order DMD mode at time j, N is the number of transient flowfields, and $\|\cdot\|_2$ represents the 2-norm of the matrix. Then the energy proportion η_i of the *i*th order DMD mode is defined as

$$\eta_i = E_i / \sum_{i=1}^N E_i. {(5.2)}$$

Figure 15 shows the distribution of energy proportions and frequencies, where the black dots are convergent or stable modes, and the red dots are unstable modes. For stages I, II and III, as the frequency increases, the energy proportion of modes decreases within the frequency range 0–12 500 Hz, but with a brief increase between 4000 and 6000 Hz, followed by a slow rise after 12 500 Hz. At stage IV, the energy proportion exhibits a slow decline with frequency, followed by a slow rise after 12 500 Hz, with stable modes occupying the majority of the energy. Overall, the energy proportion of modes decreases with increasing frequency across all four stages, but the decline is most gradual at stage IV.

To quantitatively describe the instability characteristics of each stage, the total energy proportion ($\eta_{unstable}$) and the total number proportion ($N_{unstable}$) of all unstable modes are analysed and compared, as shown in figure 16. At stage I, the total energy proportion of unstable modes is 27.3 %, with a corresponding proportion 35.9 % in number. At stage II,

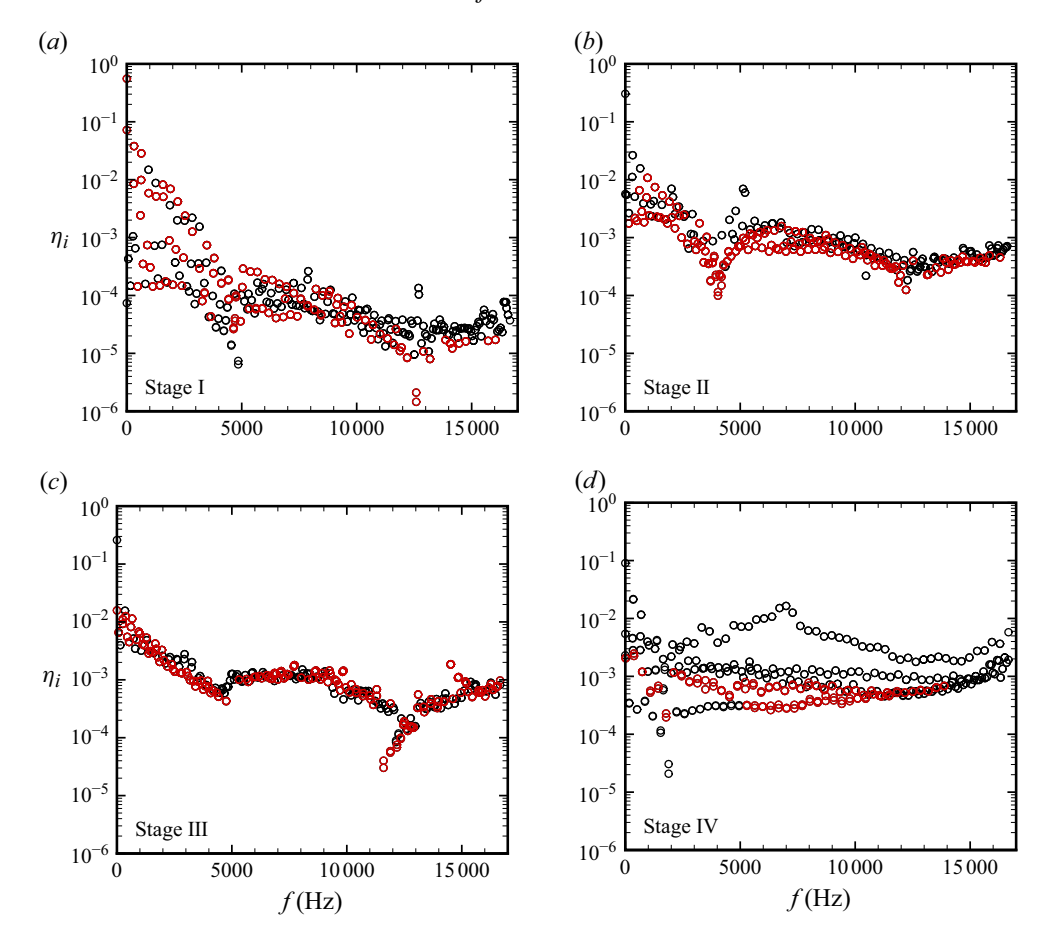


Figure 15. Distributions of mode energy proportions and frequencies.

the total energy of unstable modes is 28.2 %, which is close to that of stage I, but the number proportion increases substantially to 51.6 %. The energy of the low-frequency unstable modes is reduced, and the energy of most high-frequency unstable modes is higher than that in stage I (see figure 15). This is related to high-frequency oscillations of pressure pulsations at stage II. At stage III, the energy of unstable modes sharply increases to 45.2 %, with a corresponding increase in number to 53.6 %. Under the influence of unstable modes with large energy, the flowfield becomes unstable within a short period. Finally, at stage IV, the energy of unstable modes decreases sharply to 7.3 %, with the number decreasing to 24.3 %. Stable modes dominate the majority of the energy, leading to periodic stable oscillations in the flowfield.

The energy proportion of each mode represents its contribution to the evolution of the unsteady flowfield. Table 1 and figure 17 present the characteristic parameters and pressure gradient distributions of the maximum energy unstable modes for the four stages. Combined with the above analysis, the dominant mechanism of the unstable mode can be identified.

Before instability (stages I and II), the dominant role of unstable modes, driven by plate FSI, intensifies along with the growth of flow oscillations. At stage I, the modal structure in figure 17(a) primarily consists of the reflected shocks and shock train within the isolator, reflecting the flow characteristic of slight oscillation. The dominant frequency of the

Stage	$\text{Re}(\log(\mu_i))$	η_i	f(Hz)
I	4.512×10^{-4}	3.80 %	316.1
II	7.384×10^{-4}	1.08 %	968.1
III	1.399×10^{-4}	1.26 %	380.7
IV	4.812×10^{-4}	0.25 %	345.1

Table 1. Characteristic parameters of the maximum energy unstable modes.

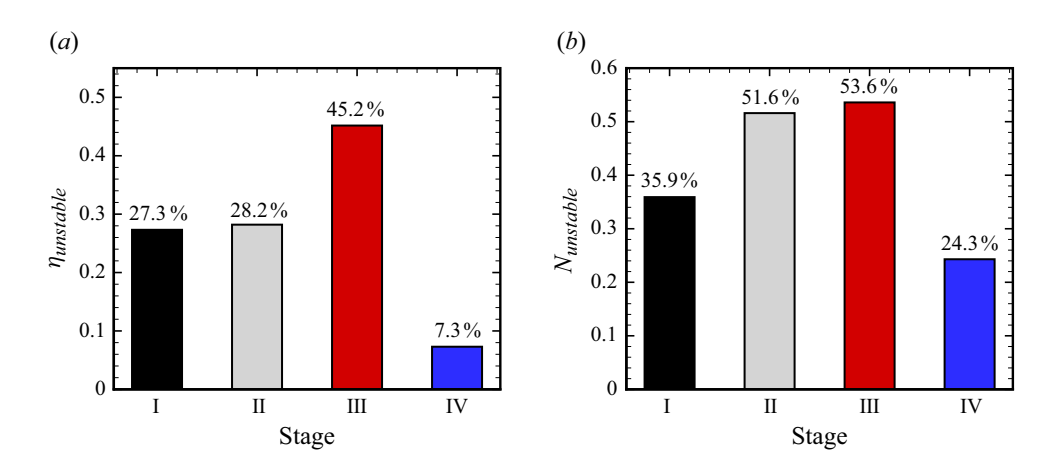


Figure 16. Total proportions of unstable modes.

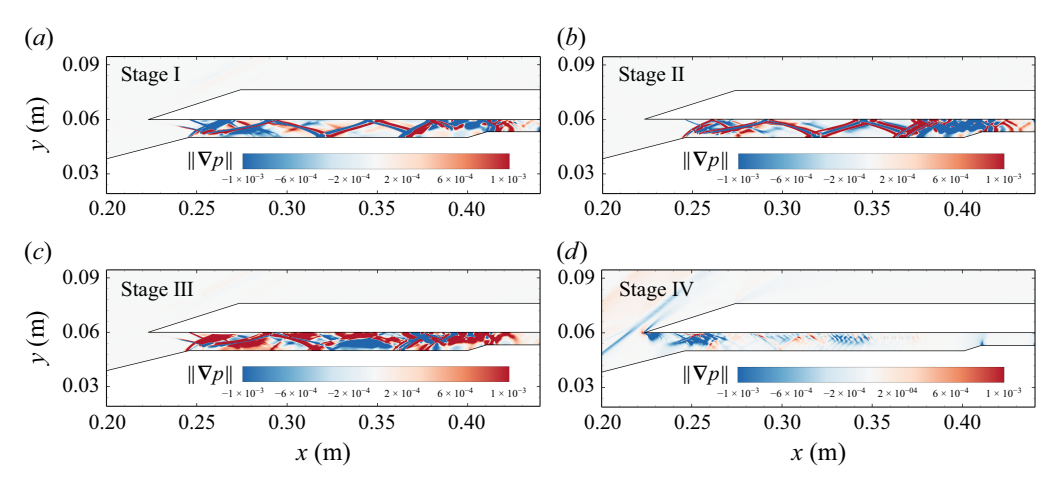


Figure 17. Pressure gradient distributions of the maximum energy unstable modes.

unstable mode is close to that of the flow oscillation, approximately 316 Hz. The plate FSI acts as the primary driver of downstream flow oscillations, effectively leading to the generation of unstable modes. Due to the nature of supersonic flow, the plate oscillations are not significantly influenced by feedback from the downstream flow. Thus during stages I and II, the plate oscillations continuously drive the strengthening of downstream flow oscillations at an approximately constant growth rate, resulting in a relatively stable level of unstable mode energy (approximately 27% in figure 16) across these two stages, as

shown in figure 15(a). The plate FSI promotes the continuous accumulation of flow instability. Unlike in stage I, during stage II, as the downstream shock train interacts with the background shocks, shock train oscillations exhibit jumps and shape changes, as shown in figure 17(b). During this process, referring to figure 15(b) and 16(b), new high-frequency instability sources are introduced into inlet flow, leading to a notable increase in high-frequency unstable modes with low modal energy. The dominant frequency of the unstable mode is 968.1 Hz, close to the third-order harmonic frequency of the flow oscillations. Meanwhile, the total unstable energy also shows a moderate rise. This indicates a further strengthening of the dominant role of unstable modes.

Entering instability (stages III and IV), the dominant unstable modes reach a shortlived energy peak, followed by a rapid decay. At stage III, by combining the flowfield with the time-domain data, it can be inferred that under the cumulative effects of unstable modes in the previous stages, the instability of the flowfield reaches a critical threshold. In figure 17(c), the shock train can no longer maintain the balance between upstream and downstream flow, and quickly destabilises, being disgorged from the inlet. During this stage, the interaction between the reflected shocks and the upstream propagating shock train further intensifies the instability of the flow. As a result, the total energy of the unstable modes surges sharply. It is noteworthy that as the destabilised shock train sweeps across the plate, it excites large-amplitude plate oscillations. This indicates that the dominant driver of flow instability transitions from plate FSI to the intrinsic instability of the flow system itself. After buzz, the flow gradually evolves into a stable periodic oscillation in figure 17(d). Due to the periodic disgorging and swallowing of the internal shock system, unstable modes can no longer continuously affect the flowfield. Instead, they are progressively replaced by the oscillatory mode of buzz. The frequency of the unstable mode is 345.1 Hz, consistent with that of buzz, with energy proportion 0.25 %, which is significantly lower than in the first three stages. Consequently, the unstable energy significantly decreases, and the influence of unstable modes is substantially suppressed. The flow oscillations tend towards a more regular periodic behaviour, indicating that the dominant role of unstable modes weakens after buzz.

Overall, before instability, the unstable mode generated by the plate FSI dominates the continuous instability of the flowfield. The violent oscillation generated by the interaction between the downstream shock train and the background wave strengthens the dominant role of the unstable mode. After instability, the shock train moves rapidly upstream, and the interaction with the background wave causes a sharp increase in the instability of the flowfield. Meanwhile, the main driving factor of flow instability has shifted from the plate FSI to the inherent instability of the flow system itself. When buzz occurs, the original unstable mode cannot continuously act in the periodic violent flow oscillation, resulting in a sharp weakening of the dominant role of the unstable mode.

6. Effect of FSI on buzz characteristics

The preceding analysis has revealed the complete evolution process of inlet buzz under plate FSI. Unlike previous studies, plate FSI exhibits a gradual-onset characteristic, accompanied by a continuous accumulation of unstable energy. To investigate the change of buzz characteristics under such conditions, this section focuses on analysing the specific effects of plate FSI on buzz characteristics, with an emphasis on comparing the similarities and differences between plate FSI buzz and rigid inlet buzz. We conducted a comparative analysis covers three aspects: pressure gradient distributions, pressure pulsations and performance parameters.

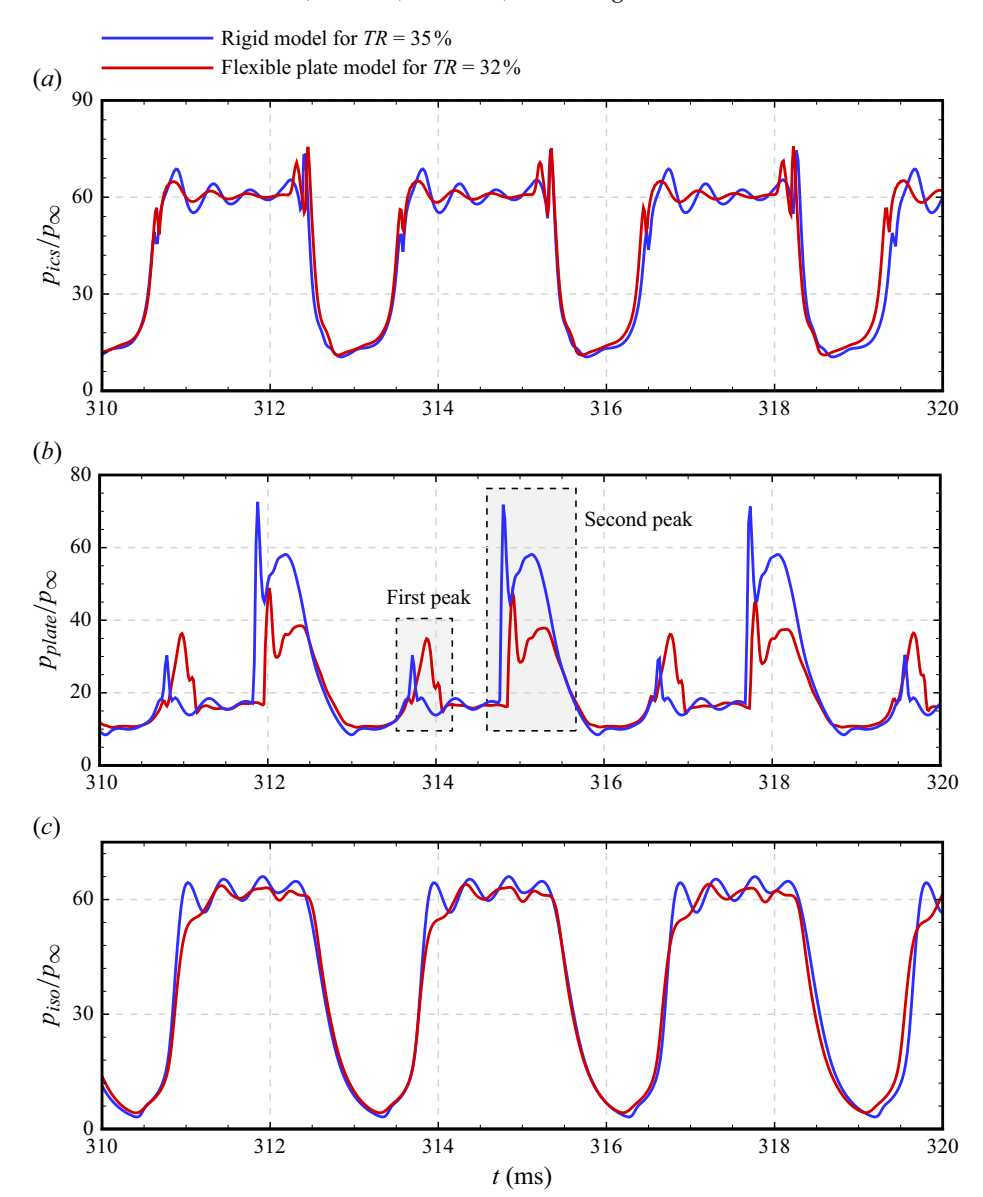


Figure 18. Comparison of pressure pulsations between rigid inlet buzz and flexible plate FSI buzz.

According to the pressure gradient distributions of the flowfield, combined with figures 13 and 23, the difference in flow characteristics mainly appears near the plate. In the vicinity of the plate under FSI, oblique shocks and expansion waves alternately appear on the upper wall. On the lower wall, more small separated bubbles appear when the shock train moves towards the plate (figure 13 6, figure 23). Further, for the plate FSI buzz, the reflected shocks within the inlet are alternately composed of the plate oblique shock and the shoulder reattachment shock (figure 13 4, 5).

The difference in the flow structure near the plate is also reflected in the pressure pulsations. Figure 18 compares the pressure pulsations at three monitoring points during buzz between the rigid inlet and the flexible plate inlet. The oscillation trends of pressure

	Rigid model for $TR = 35 \%$			Flexible plate model for $TR = 32 \%$		
	Maximum	Minimum	Amplitude	Maximum	Minimum	Amplitude
p_{ics}	75.0318	10.5099	64.5219	75.939 (1.21 %)	10.997 (4.63 %)	64.942 (0.65 %)
p_{plate}	72.9291	8.4149	64.5142	49.920 (31.55 %)	10.453 (24.22 %)	39.467 (-38.83 %)
Disc	66.0153	3.1462	62.8691	64.026 (-3.01 %)	4.188 (33.11 %)	59.838 (-4.82%)

Table 2. Comparison of extreme values and amplitudes of pressure pulsations during buzz between rigid inlet and flexible plate inlet.

pulsations at the lip (p_{ics}) and the plug (p_{iso}) are basically the same, with comparable amplitude levels. When the shock train moves upstream, the pressure within the isolator reaches a high level. At this time, their high-frequency oscillation characteristics exhibit slight differences. The pressure pulsation at the middle point of the plate (p_{plate}) shows significant differences near the two peaks. Influenced by the oblique shock generated by the convex downward deformation of the plate, the first peak value is slightly larger than that of the rigid model results. The second peak is much smaller due to the expansion wave generated by the concave upward deformation of plate and the subsequent larger separation bubble.

In addition, in order to quantitatively analyse the influence of FSI on buzz characteristics, a comparative analysis focusing on the values of pressure pulsations and performance parameters is adopted.

In terms of frequency, the pressure pulsation frequency under the FSI model is 345.9 Hz, which is close to 341.6 Hz observed for the rigid model. To show the difference in amplitude, table 2 provides a comparison of extreme values and amplitudes of pressure pulsations during buzz between rigid inlet and flexible plate inlet. Furthermore, using the rigid model as a reference, the rates of change of the time-domain characteristics at each monitoring point are calculated. The pressure pulsation characteristics at the lip (p_{ics}) exhibit minimal changes, which are similar to those of the rigid model. At the plug (p_{iso}) , both the maximum value and amplitude of pressure pulsation slightly decrease compared to the rigid model, while the minimum value increases. For the pressure pulsation at the midpoint of the plate (p_{plate}) , both the maximum value and amplitude show significant reductions of 31.55 % and 38.83 %, respectively. However, the minimum value at this point shows a significant increase of 24.22 %. This indicates the changes brought by the plate under FSI on the characteristics of the nearby flow.

In order to evaluate the effect of buzz on inlet performance, three performance parameters – flow coefficient φ , total pressure recovery coefficient σ , and pressure rise ratio R_P (Ye et al. 2019, 2024) – are introduced. The σ and R_P values are calculated by the mass weighting method. Specific definitions are

$$\varphi = \frac{\dot{m}}{\rho_{\infty} u_{\infty} A_{in}},\tag{6.1}$$

$$\sigma = \frac{\int_{out} \rho u p_0 \, dS}{\int_{in} \rho u p_0 \, dS},$$

$$R_P = \frac{\int_{out} \rho u p \, dS}{\int_{in} \rho u p \, dS},$$
(6.2)

$$R_P = \frac{\int_{out} \rho u p \, dS}{\int_{in} \rho u p \, dS},\tag{6.3}$$

where \dot{m} is the mass flow rate at the exit of the inlet, ρ_{∞} , u_{∞} and $A_{\rm in}$ are the freestream density, freestream velocity and upwind area of the inlet, and ρ , u, p_0 and p are the local

K. Ye, Y. Guo, X. Zhou, H. Zhang and Z. Ye

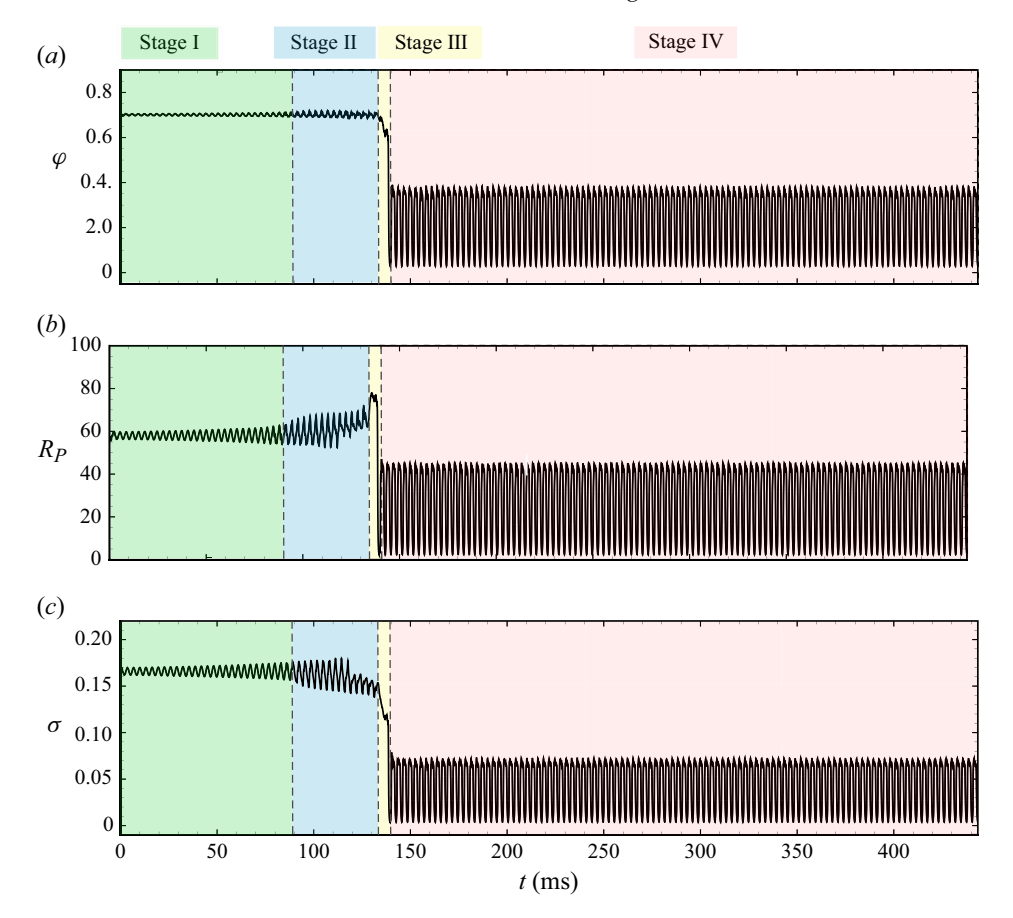


Figure 19. Time histories of performance parameters during plate FSI buzz.

density, local velocity, local total pressure and local static pressure, respectively. Subscript 'in' represents the entrance of the inlet, and subscript 'out' represents the exit.

Figure 19 presents the time histories of the flow rate coefficient, total pressure recovery coefficient and pressure rise ratio during the FSI process. The evolution of these three performance parameters over time is consistent with the evolution of pressure pulsations, covering four stages.

At stage I, all three performance parameters exhibit minor oscillations, with the amplitude slowly increasing linearly. At stage II, the amplitudes of these parameters further increase, showing a nonlinear growth trend. At stage III, all three performance parameters show a sharp decline within a relatively short period. Unlike the direct decrease in the flow rate coefficient and total pressure recovery coefficient, the pressure rise ratio initially experiences a brief increase before sharply declining. At stage IV, all three performance parameters exhibit periodic and significant oscillations over time.

Table 3 presents a comparison of extreme values and amplitudes of performance parameters during buzz between rigid inlet and flexible plate inlet. Using the rigid model as a reference, the change rates of performance parameters at stage IV are also analysed. The maximum values and amplitudes of the three performance parameters under buzz induced by FSI exhibit different trends, but the minimum values show similar increasing trends. Regarding the maximum values and amplitudes, the flow rate coefficient shows relatively minor changes. The pressure rise ratio shows a slight decrease, with reduction

	Rigid model for $TR = 35 \%$			Flexible plate model for $TR = 32\%$		
	Maximum	Minimum	Amplitude	Maximum	Minimum	Amplitude
φ	0.378	0.022	0.356	0.383 (1.26%)	0.030 (33.33 %)	0.354 (-0.72 %)
σ	47.058	1.770	45.288	45.350 (-3.63 %)	2.374 (34.16%)	42.976 (-5.11 %)
R_{D}	0.080	0.003	0.077	0.073 (-9.58%)	0.004 (34.39 %)	0.069 (-11.17%)

Table 3. Comparison of extreme values and amplitudes of performance parameters during buzz between rigid inlet and flexible plate inlet.

rates 3.63 % and 5.11 %, respectively. The total pressure recovery coefficient exhibits a significant decrease, with reduction rates 9.58 % and 11.17 %, respectively. In terms of percentages, the performance parameters have not undergone drastic changes.

In summary, compared with the rigid inlet buzz, plate FSI does not introduce significant changes to the flowfield characteristics, pressure pulsations or performance parameters. Unlike lip FSI, which has a pronounced impact on performance and pressure pulsations, the variations observed in this study are relatively modest. Since the buzz frequency under FSI is very close to that of the rigid inlet, and the associated parameter changes are not drastic, the buzz observed in this work can be classified as a mild buzz mode, as previously defined by Ye *et al.* (2024). Although the resulting buzz ultimately exhibits features similar to those observed in conventional rigid inlets, the introduction of FSI alters the local response mechanism near the flexible plate.

Therefore, although the plate FSI can also trigger buzz, its impact on the overall buzz characteristics is relatively limited compared to previous studies.

7. Conclusions

Previous studies have shown that lip FSI represents a newly identified factor capable of triggering buzz. This study further reveals the core role of FSI in the buzz evolution. By employing a flexible plate model within a hypersonic inlet, the influence of plate FSI on buzz evolution is investigated. The main findings are as follows.

Under the core influence of FSI, the buzz evolution exhibits a gradual-onset characteristic. Unlike previous studies where inlet buzz is triggered by altering the flow conditions at the rigid inlet entrance or exit, the plate FSI can drive a stable flowfield into a buzz state without changing either boundary. This finding reveals that internal FSI is a critical mechanism capable of inducing buzz. In contrast to the 'abrupt-onset' buzz commonly observed in earlier studies, the buzz under plate FSI is initiated by an instability accumulation process driven by FSI behaviour, ultimately resulting in complete flow instability. As a result, the buzz evolution under plate FSI exhibits distinct gradual-onset characteristics.

This gradual-onset buzz demonstrates a clear multistage evolution. According to the flowfield, the process can be divided into two major parts: an instability accumulation process dominated by FSI, and a complete instability process dominated by buzz. In the instability accumulation process, the plate undergoes small oscillations with increasing amplitude, driving dynamic responses in the downstream shock train. This process includes a linear development stage and a nonlinear development stage. In the linear stage, the shock train oscillates back and forth along the wall in sync with the plate oscillation. The plate oscillations continuously drive the strengthening of downstream flow oscillations. The plate FSI promotes the continuous accumulation of flow instability. As the shock train interacts with the reflection point of the background shock system, it begins

to switch periodically between symmetric and asymmetric shapes, marking the transition to the nonlinear development stage. New high-frequency instability sources are introduced into the downstream region, leading to a notable increase in high-frequency unstable modes with low modal energy. This leads to a further strengthening of the dominant role of unstable modes. Once it exceeds a critical threshold, the shock train can no longer maintain upstream—downstream balance, and the system transitions into the complete instability process. In the transition stage, the shock train is disgorged from the inlet, causing a sharp increase in plate vibration amplitude. This marks the transition of dominance between plate FSI and flow system. Subsequently, the flow enters the buzz stage, where the buzz dynamics dominates the inlet flow and in turn drives high-amplitude oscillations of the plate. Eventually, the interaction between the buzz flow and the plate's dynamic response reaches a new balance, forming a stable periodic buzz state within the inlet.

Overall, the plate FSI introduces a prolonged instability accumulation process into the buzz evolution. During this process, unstable energy generated by FSI continuously accumulates until a critical threshold is reached. Once the energy is released, the system undergoes a complete instability process, and the interaction between the flow and structure results in a stable, periodic buzz. Interestingly, this release of instability energy and internal FSI action does not significantly alter the fundamental characteristics of buzz. The plate FSI mainly affects the local flow response near the flexible plate, while the final buzz state retains the same unsteady and nonlinear characteristics as in rigid inlet buzz, showing a typical mild buzz pattern.

Therefore, plate FSI acts as an internal, self-excited disturbance source that is widely present in inlet designs. While its impact is weaker than direct flow condition changes, it exhibits a highly persistent accumulation effect and a distinct multistage evolutionary pattern. This study provides new insights into the mechanisms of buzz initiation, and offers valuable guidance for the structural design and instability control strategies of hypersonic inlets.

Supplementary movies. Supplementary movies are available at https://doi.org/10.1017/jfm.2025.10726.

Funding. This research is sponsored by the National Natural Science Foundation of China (grant nos 12422211, 12272306, U2341241, 62175243, 52175510), the 111 project of China (no. B17037), and the Fundamental Research Funds for the Central Universities of China under grant no. D5000240213.

Declaration of interests. The authors report no conflict of interest.

Appendix A. Grid convergence study and time step test

Complex shock structures exist in the internal flowfield of a hypersonic inlet. Consequently, the number and distribution of grids have a great influence on CFD calculation results. In order to simulate the inlet flowfield accurately, three sets of structured grids with grid cell numbers 70 000, 140 000 and 210 000 are adopted to verify the grid convergence. For the steady flow with TR = 32%, figure 20 shows the comparison of dimensionless pressure distributions on the lip and ramp sides with different grids. The pressure distributions across the three grid sets are largely consistent, and converge towards the results of the dense grid. Furthermore, the locally magnified results indicate that the medium grid results closely match those of the dense grid. For the FSI flow with TR = 32%, figure 21(a) shows the time histories of the midpoint displacements of the plate under three sets of grids. The results of medium mesh are basically consistent with those of dense mesh. Therefore, considering both the calculation accuracy and efficiency comprehensively, this study adopts the medium number grids with 140 000 cells for calculation in the subsequent research.

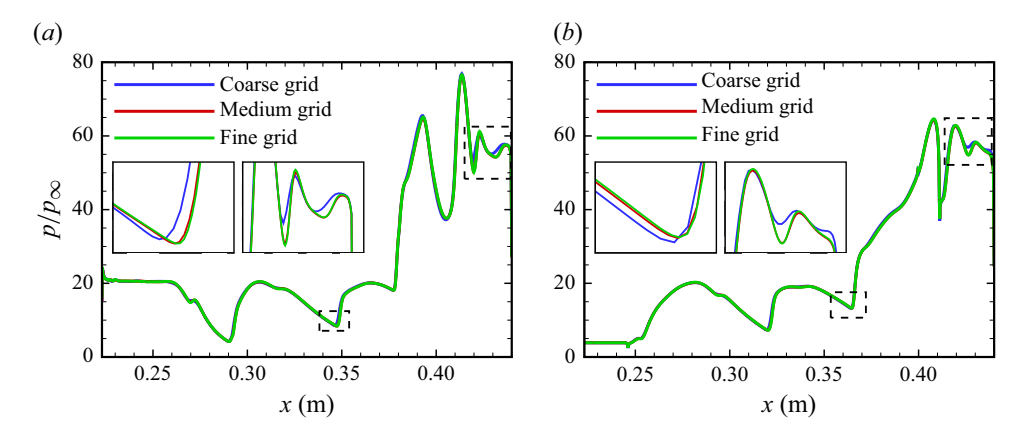


Figure 20. Comparison of pressure distributions on (a) the lip side and (b) the ramp side for different grids.

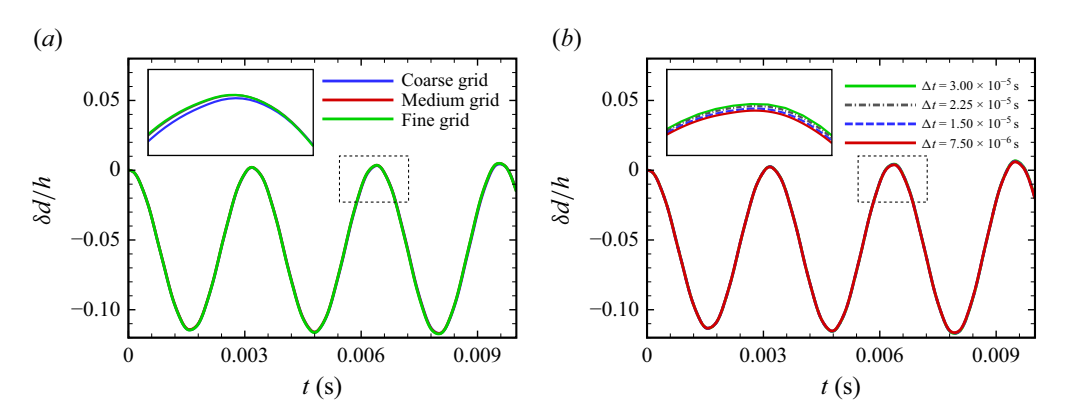


Figure 21. Time histories of displacements for different (a) grids and (b) time steps.

The time step in numerical simulation of FSI often significantly affects the accuracy of unsteady process calculations. To accurately simulate the unsteady FSI process, this study conducted convergence verification of the time step for the inlet FSI calculations with TR = 32 %, using four different time steps: 7.50×10^{-6} , 1.50×10^{-5} , 2.25×10^{-5} and 3.00×10^{-5} s. The corresponding numbers of time steps within one cycle for the four time steps are 467, 234, 156 and 117, respectively. Figure 21(b) compares the displacements of the midpoint of the plate (d_{plate}), indicating good agreement among the results obtained using the four time steps, showing that the pressure pulsation trends for the four time steps are basically consistent, with a better fit between 234 and 467 steps within one cycle. Considering both computational efficiency and accuracy, a time step 1.50×10^{-5} s is adopted for the calculations.

Appendix B. Buzz in the rigid inlet

To understand the characteristics of buzz flow, the inlet flowfield for TR = 35% is analysed. For a higher throttling ratio, the inlet flowfield becomes unstable, ultimately leading to buzz. After buzz occurs, pressure pulsations at all three monitoring points $(p_{ics}, p_{plate}, p_{iso})$ exhibit significant periodic pulsations. The dominant frequency of buzz is 341.6 Hz.

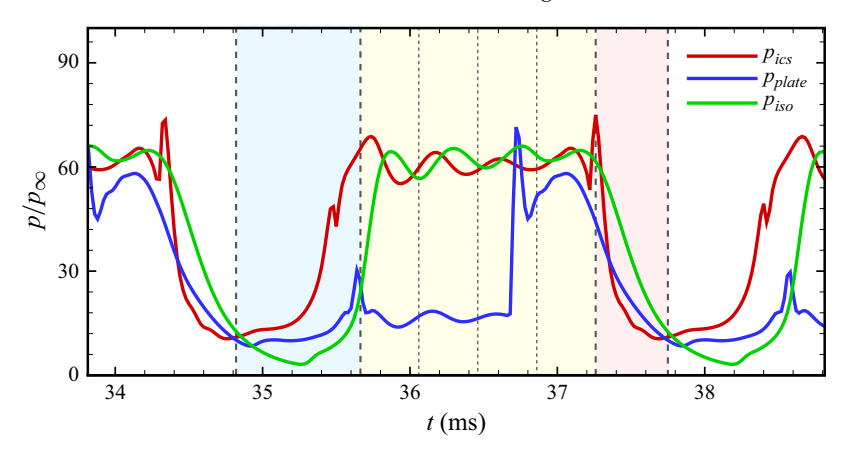


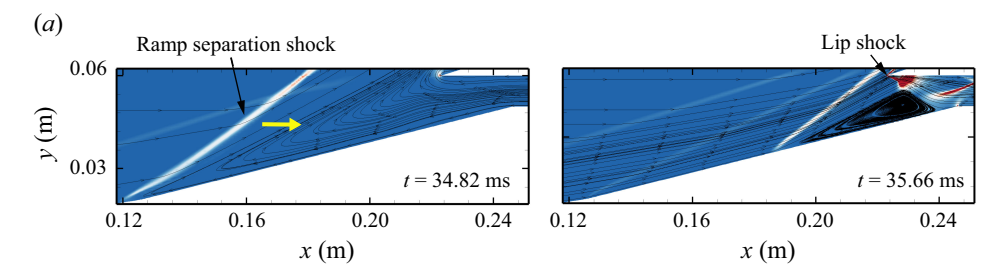
Figure 22. Pressure time histories in a typical rigid inlet buzz cycle.

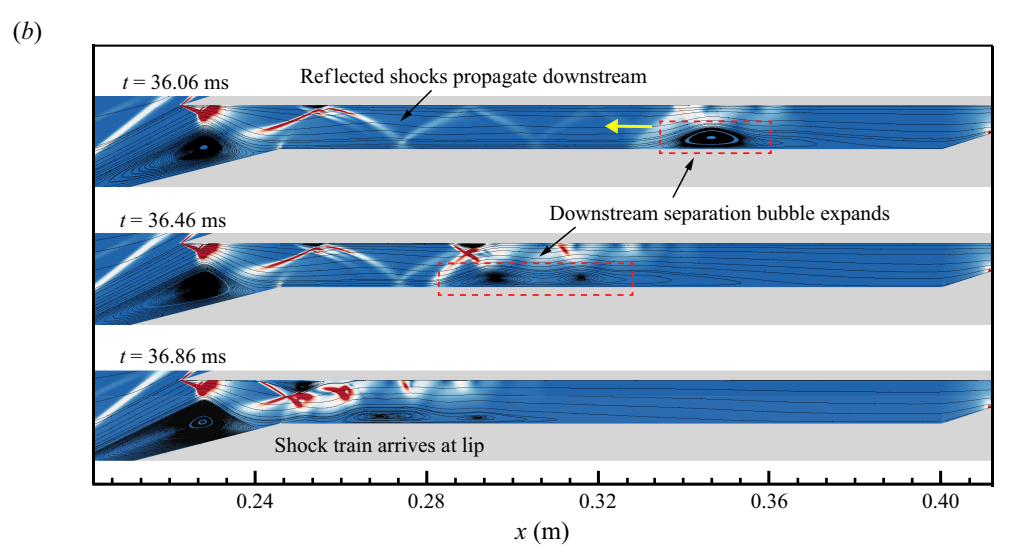
In order to investigate the evolution of the flowfield structure during buzz, a typical buzz cycle is selected for detailed analysis. According to the characteristics of pressure pulsations and shock motion, a typical buzz cycle consists of three stages: ramp separation shock close to the lip, shock train in the isolator, and ramp separation shock away from the lip.

Figure 22 presents the pressure pulsation history over a typical buzz cycle, with different colours highlighting the three stages within the cycle. To clearly illustrate the typical buzz flow characteristics, several representative time instants are selected, as indicated by the dashed lines in figure 22. Figure 23 presents the pressure gradient distributions of the flowfield during a typical buzz cycle. In figure 23(a), from t = 34.82 ms to t = 35.66 ms, the ramp separation shock moves downstream, and the airflow spillage transforms into a separation region. As the separation shock approaches the lip, it triggers the formation of a cowl shock. The lip shock causes the internal pressure $(p_{ics}, p_{plate}, p_{iso})$ of the inlet to gradually increase, marking the onset of the internal shock system formation. In figure 23(b), from t = 35.66 ms to t = 37.26 ms, the reattachment shock at the lip reflects and propagates downstream, while the separation bubble near the plug, induced by back pressure, moves upstream. During its movement, the separation bubble continuously expands, and upon interacting with the reflected shock, it forms a well-defined shock train structure. Eventually, the shock train reaches the lip and is disgorged from the inlet. During this stage, the internal pressure fluctuates continuously. In figure 23(c), from t = 37.26ms to t = 37.74 ms, the internal shock structures within the inlet completely disappear, and the separation region near the shoulder rapidly expands, pushing the ramp separation shock upstream. Subsequently, a large-scale spillage occurs at the shoulder, with the ramp separation shock reaching its most upstream position, accompanied by a sharp drop in internal pressure. The buzz is about to enter a new cycle.

Figure 24 shows the time histories of the flow coefficient, total pressure recovery coefficient, and pressure rise ratio for TR = 35%. After the occurrence of buzz, all three performance parameters exhibit significant periodic oscillations (Ye *et al.* 2024). Both the flow coefficient and total pressure recovery coefficient decrease after buzz, indicating that the air mass flow and work capacity of the inlet significantly decrease. For the pressure rise ratio, the value increases after buzz, with a large amplitude.

Overall, for the rigid inlet model, throttling ratio 34 % represents the critical throttling ratio for buzz. When the throttling ratio is below this critical value, the flowfield remains stable. However, when the throttling ratio exceeds the critical value, the inlet flowfield





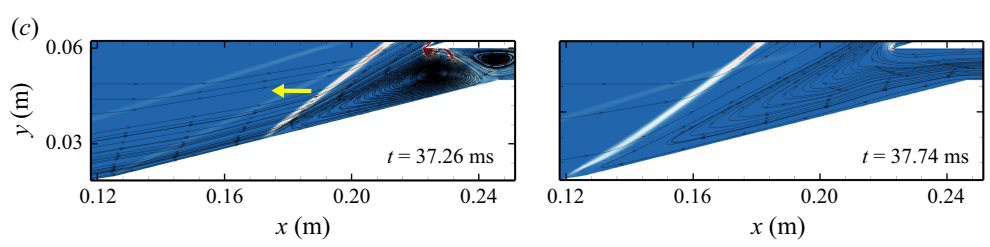


Figure 23. Pressure gradient distributions of flowfield during a typical buzz cycle.

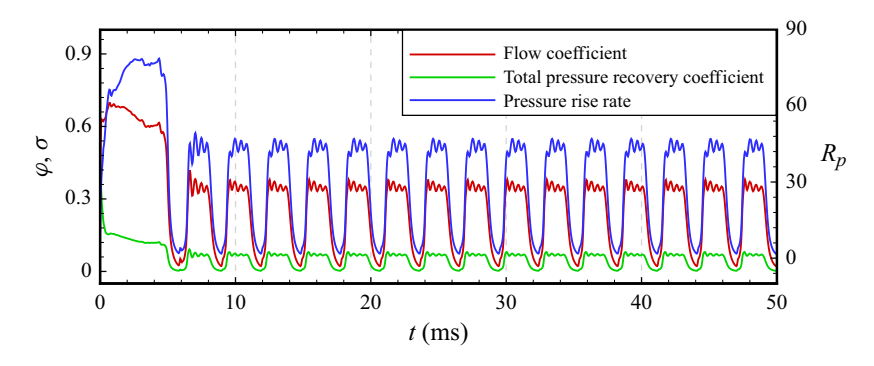


Figure 24. Time histories of performance parameters for TR = 35%.

becomes unstable, with periodic oscillations characterised by the flow structures being periodically disgorged and swallowed. This instability leads to significant oscillations in both pressure and performance parameters, indicating the occurrence of buzz. This unstable oscillatory flow was mentioned in the studies by Tan *et al.* (2009) and Li *et al.* (2013).

Appendix C. The DMD method

The data for the DMD method (Jovanović *et al.* 2014) mainly come from numerical simulations or experiments, presented in the form of a sequence of snapshots arranged in chronological order. The sequence is represented by a matrix

$$V_1^N = \{ v_1, v_2, v_3, \dots, v_N \},$$
 (C1)

where v_i represents the flowfield at the *i*th instant, $v_i \in C^M$. Here, C^M is an M-dimensional complex vector space. In the above definition, the subscripts 1 and N represent the flowfields at the first and last instants, respectively, with time interval Δt between snapshot sequences.

Assuming that there is a linear mapping between the flow snapshot v_i at time i and the flow snapshot v_{i+1} at the next time, i.e.

$$\mathbf{v}_{i+1} = A\mathbf{v}_i,\tag{C2}$$

if all flow areas sampled over the entire time period satisfy this mapping relationship, then

$$V_1^N = \{v_1, v_2, v_3, \dots, v_N\} = \{Av_0, Av_1, Av_2, \dots, Av_{N-1}\} = AV_0^{N-1}.$$
 (C3)

The system matrix A can shift the time—space physical field along the time dimension by Δt , so the eigenvalues of the system matrix A represent the time evolution characteristics of V_1^N . In practical physical problems, the system matrix A is often a high-order two-dimensional square matrix, making the computation of its eigenvalues challenging. Therefore, it is necessary to transform the system matrix A into a smaller matrix K, and use the eigenvalues of the smaller matrix K to estimate the eigenvalues of the system matrix A, thus enabling the use of the DMD method to solve actual dynamics problems.

For the data column V_0^{N-1} with rank r, the system matrix A and its simplified smaller matrix $K \in C^{r \times r}$ can be related through the proper orthogonal decomposition (POD) modes of V_0^{N-1} as

$$A \approx TKT^*$$
, (C4)

where T^* is the complex conjugate transpose matrix of POD modes T, which can be obtained from the singular value decomposition (SVD) of the snapshot sequence V_0^{N-1} , namely,

$$V_0^{N-1} = T \Sigma V^*, \tag{C5}$$

where Σ is an $r \times r$ diagonal matrix with non-zero diagonal elements, and

$$T \in C^{M \times r}, \quad T^*T = I,$$
 (C6)

$$V \in C^{r \times N}, \quad V^*V = I.$$
 (C7)

Substituting (C4) and (C5) into (C3), it can be obtained that

$$K = T^* V_1^N V \Sigma^{-1}, \tag{C8}$$

where K is the optimal low-dimensional estimation matrix, thus the results of the DMD analysis can be obtained by calculating the eigenvalues and eigenvectors of K.

Assume that $K \in C^{r \times r}$ is a precise mapping matrix in an r-dimensional subspace, not an estimate of $A \in C^{M \times M}$. Then

$$\boldsymbol{x}_{k+1} = \boldsymbol{K}\boldsymbol{x}_k, \tag{C9}$$

hence the matrix of POD modes U can be seen as an approximate mapping from x_k to v_k , i.e.

$$\mathbf{v}_k \approx T \mathbf{x}_k$$
. (C10)

If **K** has a full set of linearly independent eigenvectors $Y = \{y_1, \ldots, y_r\}$, with corresponding eigenvalues $D_{\mu} = \{\mu_1, \ldots, \mu_r\}$, then it can be brought into a diagonal coordinate form

$$\mathbf{K} = \begin{bmatrix} \mathbf{y}_1 \cdots \mathbf{y}_r \end{bmatrix} \begin{bmatrix} \mu_1 \\ \vdots \\ \mu_r \end{bmatrix} \begin{bmatrix} \mathbf{z}_1^* \\ \vdots \\ \mathbf{z}_r^* \end{bmatrix}. \tag{C11}$$

The modulus of each y_i is a unit length, i.e. $y_i^*y_i = 1$, $Z = \{z_1, \ldots, z_r\}$ are the eigenvectors of K^* , and the corresponding eigenvalues of K^* are $\{\overline{\mu}_1, \ldots, \overline{\mu}_r\}$. Furthermore, z_i^* and y_i satisfy the conditions

$$\boldsymbol{z}_{i}^{*}\boldsymbol{y}_{j} = \begin{cases} 1, & i = j, \\ 0, & i \neq j. \end{cases}$$
 (C12)

Then the solution to (C9) is determined by

$$\mathbf{x}_{k} = \mathbf{Y} \mathbf{D}_{\mu}^{k} \mathbf{Z}^{*} \mathbf{x}_{0} = \sum_{i=1}^{r} \mathbf{y}_{i} \mu_{i}^{k} \mathbf{z}_{i}^{*} \mathbf{x}_{0} = \sum_{i=1}^{r} \mathbf{y}_{i} \mu_{i}^{k} \alpha_{i},$$
 (C13)

where $\alpha_i = z_i^* x_0$ represents the influence of initial conditions on the *i*th mode, therefore the linear combination of DMD modes can be used to estimate the data snapshot, and the mode is $\Phi_i = T y_i$; i.e.

$$\mathbf{v}_k \approx \mathbf{T} \mathbf{x}_k = \sum_{i=1}^r \boldsymbol{\phi}_i \mu_i^k \alpha_i. \tag{C14}$$

Thus it can be obtained that

$$[\mathbf{v}_0, \mathbf{v}_2, \dots, \mathbf{v}_{N-1}] \approx [\boldsymbol{\phi}_1, \boldsymbol{\phi}_2, \dots, \boldsymbol{\phi}_r] \begin{bmatrix} \alpha_1 & & & \\ & \alpha_2 & & \\ & & \ddots & \\ & & & \alpha_r \end{bmatrix} \begin{bmatrix} 1 & \mu_1 & \dots & \mu_1^{N-1} \\ 1 & \mu_2 & \dots & \mu_2^{N-1} \\ \vdots & \vdots & \ddots & \vdots \\ 1 & \mu_r & \dots & \mu_r^{N-1} \end{bmatrix} .$$

$$(C15)$$

The most important result obtained by the DMD method is the mode ϕ_i and the corresponding eigenvalue μ_i . The real part of $\log \mu_i/\Delta t$ is the magnification of the corresponding mode, and the imaginary part represents the frequency of the corresponding mode. In the stability judgement process, if the magnification is positive, then the corresponding mode diverges. If the magnification is negative, then the corresponding mode converges. And if the magnification is 0, then the corresponding mode is the stable

K. Ye, Y. Guo, X. Zhou, H. Zhang and Z. Ye

limit cycle mode. This can also be judged by checking the position of μ_i on the unit circle of the complex plane. If it is in the unit circle, then the mode converges. If it is outside the unit circle, then the mode diverges, and if it is on the unit circle, then it turns to be a stable periodic mode.

REFERENCES

- ABEDI, M., ASKARI, R. & SOLTANI, M.R. 2020 Numerical simulation of inlet buzz. *Aerosp. Sci. Technol.* 97, 105547.
- BACCARELLA, D., LIU, Q., MCGANN, B., LEE, G. & LEE, T. 2021 Isolator-combustor interactions in a circular model scramiet with thermal and non-thermal choking-induced unstart. *J. Fluid Mech.* 917, A38.
- BERTO, F., BENINI, E., WYATT, C. & QUINN, M.K. 2020 Time-accurate experimental investigation of hypersonic inlet buzz at Mach 5. AIAA J. 58 (5), 2197–2205.
- BHATTRAI, S., McQUELLIN, L.P., CURRAO, G.M.D., NEELY, A.J. & BUTTSWORTH, D.R. 2022 Experimental study of aeroelastic response and performance of a hypersonic intake ramp. *J. Propul. Power* 38 (1), 157–170.
- BOYER, N.R., McZNAMARA, J.J., GAITONDE, D.V., BARNES, C.J. & VISBAL, M.R. 2018 Features of shock-induced panel flutter in three-dimensional inviscid flow. *J. Fluid Mech.* 83, 490–506.
- Brenner, S.C. & Scott, L.R. 2008 The Mathematical Theory of Finite Element Methods. Springer.
- BROUWER, K.R., PEREZ, R.A., BEBERNISS, T.J., SPOTTSWOOD, S.M. & EHRHARDT, D.A. 2021 Experiments on a thin panel excited by turbulent flow and shock/boundary-layer interactions. *AIAA J.* **59** (7), 2737–2752.
- CHANG, J., WANG, L., BAO, W., QIN, J., NIU, J. & XUE, W. 2012 Novel oscillatory patterns of hypersonic inlet buzz. J. Propul. Power 28 (6), 1214–1221.
- CHANG, J., ZHANG, J., BAO, W. & YU, D. 2018 Research progress on strut-equipped supersonic combustors for scramjet application. *Prog. Aerosp. Sci.* 103, 1–30.
- DAUB, D., WILLEMS, S. & GÜLHAN, A.2016 Experiments on the interaction of a fast-moving shock with an elastic panel. AIAA J. 54 (2), 670–678.
- DEVARAJ, M.K.K., JUTUR, P., RAO, S.M.V., JAGADEESH, G. & ANAVARDHAM, G.T.K. 2020 Experimental investigation of unstart dynamics driven by subsonic spillage in a hypersonic scramjet intake at Mach 6. *Phys. Fluids* 32 (2), 026103.
- DEVARAJ, M.K.K., JUTUR, P., RAO, S.M.V., JAGADEESH, G. & ANAVARDHAM, G.T.K. 2021 Length scale for the estimation of buzz frequency in the limit of high mechanical blockage in mixed-compression intakes. *J. Fluid Mech.* **916**, R3.
- FARHAT, C. & LESOINNE, M. 2000 Two efficient staggered algorithms for the serial and parallel solution of three-dimensional nonlinear transient aeroelastic problems. *Comput. Meth. Appl. Mech. Engng* **182** (3–4), 499–515.
- GORDNIER, R.E. & VISBAL, M.R. 2002 Development of a three-dimensional viscous aeroelastic solver for nonlinear panel flutter. *J. Fluid. Struct.* **16** (4), 497–527.
- GOURA, G.S.L., BADCOCK, K.J., WOODGATE, M.A. & RICHARDS, B.E. 2001 A data exchange method for fluid-structure interaction problems. *Aeronaut. J.* 105 (1046), 215–221.
- HONG, W. & KIM, C. 2014 Computational study on hysteretic inlet buzz characteristics under varying mass flow conditions. AIAA J. 52 (7), 1357–1373.
- HONG, Z., YE, Z. & YE, K. 2023 Effect of two-dimensional micro-cavity surface on hypersonic boundary layer. Acta Astronaut. 206, 188–205.
- HUANG, H., TAN, H., CAI, J. & SUN, S. 2021 Restart processes of rectangular hypersonic inlets with different internal contraction ratios. AIAA J. 59 (7), 2427–2439.
- IM, S. & Do, H. 2018 Unstart phenomena induced by flow choking in scramjet inlet-isolators. *Prog. Aerosp. Sci.* 97, 1–21.
- JAMES, J.K., SURYAN, A. & KIM, H.D. 2021 Buzz characteristics and separation bubble dynamics in supersonic intake. Aerosp. Sci. Technol. 115, 106795.
- JOVANOVIĆ, M.R., SCHMID, P.J. & NICHOLS, J.W. 2014 Sparsity-promoting dynamic mode decomposition. Phys. Fluids 26 (2).
- KHOBRAGADE, N., UNNIKRISHNAN, S. & KUMAR, R. 2022 Flow instabilities and impact of ramp-isolator junction on shock-boundary-layer interactions in a supersonic intake. *J. Fluid Mech.* **953**, A30.
- KLINE, H., PALACIOS, F. & ALONSO, J.J. 2014 Sensitivity of the performance of a 3-dimensional hypersonic inlet to shape deformations, In *Proceedings of the 19th AIAA International Space Planes and Hypersonic Systems and Technologies Conference (AIAA AVIATION Forum), Atlanta, GA, USA.* AIAA.

- LAMORTE, N., FRIEDMANN, P.P., DALLE, D.J., TORREZ, S.M. & DRISCOLL, J.F. 2015 Uncertainty propagation in integrated airframe–propulsion system analysis for hypersonic vehicles. *J. Propul. Power* 31 (1), 54–68.
- LI, Z., GAO, W., JIANG, H. & YANG, J. 2013 Unsteady behaviors of a hypersonic inlet caused by throttling in shock tunnel. AIAA J. 51 (10), 2485–2492.
- LIAO, F., YE, Z. & ZHANG, L. 2015 Extending geometric conservation law to cell-centered finite difference methods on stationary grids. J. Comput. Phys. 284, 419–433.
- LIU, H., YAN, C., ZHAO, Y. & QIN, Y. 2018 Uncertainty and sensitivity analysis of flow parameters on aerodynamics of a hypersonic inlet. Acta Astronaut. 151, 703–716.
- PARK, Y., NAM, J., KIM, Y., JUN, D., LEE, B.J. & LEE, Y.J. 2023 Validation of numerical simulations for investigating flow control in hypersonic inlets. *Aerosp. Sci. Technol.* 140, 108452.
- REINARTZ, B.U., HERRMANN, C.D., BALLMANN, J. & KOSCHEL, W.W. 2003 Aerodynamic performance analysis of a hypersonic inlet isolator using computation and experiment. *J. Propul. Power* 19 (5), 868–875.
- ROWLEY, C.W. & DAWSON, S.T.M. 2017 Model reduction for flow analysis and control. Annu. Rev. Fluid Mech. 49, 387–417.
- SCHMID, P.J. 2010 Dynamic mode decomposition of numerical and experimental data. J. Fluid Mech. 656, 5–28.
- SHI, W., CHANG, J., WANG, Y., BAO, W. & LIU, X. 2019 Buzz evolution process investigation of a two-ramp inlet with translating cowl. *Aerosp. Sci. Technol.* **84**, 712–723.
- SHINDE, V.J., McNamara, J.J., Gaitonde, D.V., Barnes, C.J. & Visbal, M. 2018 Panel flutter induced by transitional shock wave boundary layer interaction, In *Proceedings of the 2018 AIAA Fluid Dynamics Conference (AIAA AVIATION Forum)*, Atlanta, GA, USA. AIAA.
- SZIROCZAK, D. & SMITH, H. 2016 A review of design issues specific to hypersonic flight vehicles. *Prog. Aerosp. Sci.* **84**, 1–28.
- TAN, H., LI, L., WEN, Y. & ZHANG, Q. 2011 Experimental investigation of the unstart process of a generic hypersonic inlet. AIAA J. 49 (2), 279–288.
- TAN, H., SUN, S. & YIN, Z. 2009 Oscillatory flows of rectangular hypersonic inlet unstart caused by downstream mass-flow choking. *J. Propul. Power* **25** (1), 138–147.
- VISBAL, M. 2012 On the interaction of an oblique shock with a flexible panel. J. Fluid. Struct. 30, 219-225.
- WAGNER, J.L., YUCEIL, K.B., VALDIVIA, A., CLEMENS, N.T. & DOLLING, D.S. 2009 Experimental investigation of unstart in an inlet/isolator model in Mach 5 flow. AIAA J. 47 (6), 1528–1542.
- XIONG, B., FAN, X. & WANG, Y., 2021 Design and evaluation of a conical hypersonic vehicle with an overturned aerodynamic layout. Aerosp. Sci. Technol. 118, 106979.
- XIONG, B., FAN, X., WANG, Z. & TAO, Y. 2018 Analysis and modelling of unsteady shock train motions. J. Fluid Mech. 846, 240–262.
- XU, K., CHANG, J., ZHOU, W. & YU, D. 2017 Mechanism of shock train rapid motion induced by variation of attack angle. Acta Astronaut. 140, 18–26.
- Xu, S., Wang, Y., Wang, Z., Fan, X. & & Xiong, B. 2022 Unsteady behavior of hypersonic inlet unstart caused by high angle of attack. *Aerosp. Sci. Technol.* **130**, 107884.
- YE, K., YE, Z., LI, C. & Wu, J. 2019 Effects of the aerothermoelastic deformation on the performance of the three-dimensional hypersonic inlet. Aerosp. Sci. Technol. 84, 747–762.
- YE, K., ZHANG, Y., CHEN, Z. & YE, Z. 2022 Numerical investigation of aeroelastic characteristics of grid fin. AIAA J. 60 (5), 3107–3121.
- YE, K., ZHOU, X. & YE, Z. 2024 Buzz characteristics under fluid–structure interaction of variable-geometry lip for hypersonic inlet. AIAA J. 62 (5), 1662–1682.
- YE, L. & YE, Z. 2018 Effects of shock location on aeroelastic stability of flexible panel. AIAA J. 56 (9), 3732–3744.
- ZHA, Z., YE, K. & YE, Z. 2022 Stability analysis of shock-mixing interaction based on dynamic mode decomposition. Aerosp. Sci. Technol. 123, 107492.
- ZHANG, Q., TAN, H., CHEN, H., YUAN, Y. & ZHANG, Y. 2016a Unstart process of a rectangular hypersonic inlet at different Mach numbers. AIAA J. 54 (12), 3681–3691.
- ZHANG, Q., TAN, H., SUN, S., BU, H. & RAO, C. 2016b Unstart of a hypersonic inlet with side compression caused by downstream choking. AIAA J. 54 (1), 28–38.
- ZHANG, Y., YE, K. & YE, Z. 2024 On the aeroelastic bifurcation of a flexible panel subjected to cavity pressure and inviscid oblique shock. *J. Fluid Mech.* **986**, A28.